

Master thesis and internship[BR]- Master's thesis : Computation of satellite orbits around asteroids using the ManLab software[BR]- Integration Internship : ULiège

Auteur : Majer, Riccardo

Promoteur(s) : Kerschen, Gaëtan

Faculté : Faculté des Sciences appliquées

Diplôme : Master en ingénieur civil en aérospatiale, à finalité spécialisée en "aerospace engineering"

Année académique : 2022-2023

URI/URL : <http://hdl.handle.net/2268.2/18326>

Avertissement à l'attention des usagers :

Tous les documents placés en accès ouvert sur le site le site MatheO sont protégés par le droit d'auteur. Conformément aux principes énoncés par la "Budapest Open Access Initiative"(BOAI, 2002), l'utilisateur du site peut lire, télécharger, copier, transmettre, imprimer, chercher ou faire un lien vers le texte intégral de ces documents, les disséquer pour les indexer, s'en servir de données pour un logiciel, ou s'en servir à toute autre fin légale (ou prévue par la réglementation relative au droit d'auteur). Toute utilisation du document à des fins commerciales est strictement interdite.

Par ailleurs, l'utilisateur s'engage à respecter les droits moraux de l'auteur, principalement le droit à l'intégrité de l'oeuvre et le droit de paternité et ce dans toute utilisation que l'utilisateur entreprend. Ainsi, à titre d'exemple, lorsqu'il reproduira un document par extrait ou dans son intégralité, l'utilisateur citera de manière complète les sources telles que mentionnées ci-dessus. Toute utilisation non explicitement autorisée ci-avant (telle que par exemple, la modification du document ou son résumé) nécessite l'autorisation préalable et expresse des auteurs ou de leurs ayants droit.



POLITECNICO
MILANO 1863

SCUOLA DI INGEGNERIA INDUSTRIALE
E DELL'INFORMAZIONE



Computation of satellite orbits around asteroids using the ManLab software

Master's thesis completed in order to obtain the degree of
Master of Science in Aerospace Engineering

By:

Riccardo Majer

Academic advisor at Université de Liège: Prof. G. KERSCHEN
Academic advisor at Politecnico di Milano: Prof. F. FERRARI

Faculté des Sciences Appliquées - UNIVERSITÉ DE LIÈGE
Scuola di Ingegneria Industriale e dell'Informazione - POLITECNICO DI MILANO
Academic year: 2022-2023



Acknowledgements

I would like to express my most sincere gratitude to my supervisors, Professor Fabio Ferrari and Professor Gaëtan Kerschen, for having inspired me and offered me their crucial guidance and useful critiques and to Nicolas Leclere from the evaluation committee for his dedicated time and help. I would also like to thank all the friends i met at the A&M department at ULiège, as they made the experience to be incredible. In particular I thanks Jennifer, you have been a good office mate and your contribution to this work was precious.

Prima di tutti vorrei ringraziare i miei genitori e mia sorella, mi avete sempre supportato ed è solo grazie a voi che sono arrivato fino a qui.

Ringrazio Jorge con cui ho condiviso il cammino per molti anni, e che nonostante la lontananza rimane sempre l'amico migliore che si possa avere. Ovviamente la nostra ricerca in coop della vera matematica continuerà per sempre, ci sarà sempre una nuova avventura in cui il ricercatore op deve caricare il noob.

Un grazie speciale a tutti coloro che ho conosciuto a Milano e che ho dovuto salutare. In particolare a Paolo, che più di tutti ha sopportato le mie cavolate e che ha reso gli anni della triennale più divertenti.

Infine ringrazio tutti quelli che ho avuto la fortuna di conoscere a Liège in questi due fantastici anni, ma in particolare ringrazio:

Nico, sei diventato come un fratello nonchè coinquilino ad honorem ed ogni volta che siamo insieme facciamo casino. Non ti preoccupare che prima o poi ti ci porto in Sardegna;

Simo, che senza volerlo te ne esci sempre con delle perle dalla saggezza infinita, ufficialmente il cuoco migliore del mondo. Senza di te io e Lorenzo avremmo fatto la fame;

Tecla, per avermi sopportato fin dal primo giorno e per essere stata la miglior compagna di squadra in ogni progetto;

Lorenzo, compagno di molte avventure nonchè il vero compagno d'ufficio, senza di te l'intermarchè è un luogo triste e vuoto;

Pionao, uomo Erasmus anche nell'anno successivo al tuo. Dopo la tua partenza Liège non è più la stessa;

Lollo, il compagno di banco per eccellenza, senza di te il corso di francese sarebbe stato terribilmente noioso;

Grazie di tutto.

Abstract

The computation of periodic orbits in non-Keplerian dynamics is a critical issue for space missions, mostly for those around irregular asteroids. The purpose of this thesis is to use a novel, frequency domain, approach to solve the problem. The approach is based on the Harmonic Balance Method, a well known method for the analysis of nonlinear vibrations, but never used before in astrodynamics. In this thesis, it was used the Harmonic Balance Method implemented in ManLab, an interactive path-following and bifurcation analysis software.

The study starts with a theoretical explanation about the circular restricted three body problem and about the dynamical problem around asteroids. For the latter, the available gravitational model are displayed in order to correctly select the one of interest. After this first theoretical introduction, the classical methods used in the field are briefly discussed, and the theory behind the Harmonic Balance Method and its ManLab implementation is introduced.

After this preliminary introduction the two problems are analyzed. For the circular restricted three body problem, the analysis focus on the description of the bifurcations of the families of orbits around the first Lagrangian point. For the problem around an asteroid a fictitious spherical asteroid, for which some periodic orbits were computed and compared with the ones obtained through time integration and through the classical Harmonic Balance Method.

Keywords: ManLab; Harmonic Balance Method; Asteroid dynamics; Gravitational model; Circular restricted three body problem; Periodic orbits.

Sommario

Il calcolo di orbite periodiche nella dinamica non-Kepleriana è un problema di estrema importanza per le missioni spaziali, soprattutto per quelle attorno ad asteroidi dalla forma irregolare. Lo scopo di questa tesi è quello di usare un nuovo metodo in frequenza per affrontare questo problema. Questo approccio si basa sul metodo del bilanciamento armonico, un metodo ben conosciuto nell'ambito delle vibrazioni non lineari, ma mai usato prima in astrodinamica. In questa tesi, è stata usata l'implementazione del metodo del bilanciamento armonico che è disponibile in ManLab, un programma interattivo per l'analisi delle biforcazioni di sistemi non lineari.

Lo studio inizia con un introduzione teorica riguardante il problema dei tre corpi ristretto e circolare e riguardante la dinamica attorno agli asteroidi. In particolare, per quest'ultimo, i principali modelli gravitazionali sono stati introdotti, in modo da poter selezionare il più consono per lo scopo della tesi. Successivamente, sono brevemente discussi i metodi classici che vengono utilizzati al momento per affrontare il problema. Sono introdotti inoltre sia il metodo del bilanciamento armonico classico, sia la sua implementazione in ManLab.

In seguito a questa introduzione i due problemi sono stati analizzati. Per il problema dei tre corpi ristretto e circolare, l'analisi si focalizza sulla descrizione delle biforcazioni delle famiglie di orbite attorno al primo punto Lagrangiano del sistema. Per l'analisi del problema attorno ad asteroidi è stato invece usato un asteroide sferico fittizio, per il quale alcune famiglie di orbite periodiche sono state calcolate e confrontate con quelle ottenute tramite integrazione nel tempo e tramite il metodo del bilanciamento armonico classico.

Parole chiave: ManLab; Metodo del Bilanciamento Armonico; Dinamica intorno agli asteroidi; Modelli gravitazionali; Problema dei tre corpi ristretto e circolare; Orbite periodiche.

Contents

Acknowledgements	I
Abstract	II
Sommario	III
List of Figures	VI
List of Tables	IX
Acronyms	X
1 Introduction	1
1.1 Motivation and thesis outline	1
2 Theoretical background	3
2.1 Circular restricted three-body problem.	3
2.1.1 Equilibrium points and zero velocity curves	4
2.2 Asteroid case	5
2.2.1 Equilibrium points and zero velocity curves	6
2.2.2 Gravitational potential.	7
2.3 Periodic orbit generation	13
2.3.1 The Harmonic Balance Method.	14
2.4 Stability	17
3 ManLab	20
3.1 Introduction.	20
3.2 Theory	20
3.2.1 Quadratic formulation of the Harmonic Balance Method	21
3.2.2 Asymptotic Numerical Method.	21
3.2.3 Quadratic formulation of the Floquet-Hill stability	23
3.3 Application on elementary examples	24
3.3.1 Initial conditions	24
3.3.2 Forced Van der Pol oscillator	25
3.3.3 Free nonlinear pendulum	26
4 Validation	29
4.1 Gravitational potential model	29
4.1.1 Earth gravity.	29
4.1.2 Asteroid potential.	32
4.2 ManLab	33
5 Application	38
5.1 Circular restricted three body problem	38
5.1.1 Recast.	38
5.1.2 Families around L_1 Lagrange point	39
5.2 Asteroid problem.	45
5.2.1 Recast.	45
5.2.2 Icosphere.	47

6	Conclusions and future development	53
	References	IV
A	Families around L_2 and L_3 Lagrange Point	V
A.1	Families around L_2	V
A.2	Families around L_3	VI

List of Figures

2.1	Circular restricted three-body problem system in the rotating reference frame. . . .	3
2.2	ZVC and equilibrium points of Earth-Moon system.	5
2.3	ZVC and equilibrium points of <i>1996 Hw1</i>	7
2.4	Brillouin sphere of asteroid <i>1620 Geographos</i>	9
2.5	Tri-axial ellipsoid.	9
2.6	Schematic of two faces with a common edge and their respective normal [33]. . . .	11
2.7	Polyhedron mesh of the asteroid <i>1996 Hw1</i>	12
2.8	General periodic orbit generation scheme	13
2.9	Floquet multipliers evolution on the complex plane during the various bifurcations.	19
3.1	Evolution on the complex plane of the Floquet multipliers during the continuation of the solution branch.	25
3.2	L2 Norm of the x variable.	25
3.3	Van der pol phase space evolution during the continuation.	26
3.4	Evolution on the complex plane of the Floquet multipliers during the continuation of the solution branch.	27
3.5	θ_{max} for each pulsation value.	27
3.6	Free pendulum phase space evolution during the continuation.	28
4.1	Analytical and polyhedral sea level gravitational acceleration changing the number of the vertices of the polyhedron.	29
4.2	Percentual relative error between the two methods.	29
4.3	Computation time to perform the calculation to polyhedron with different number of vertices.	30
4.4	Analytical and polyhedral gravitational acceleration comparison at different altitudes.	30
4.5	Percentual relative error between the two methods.	30
4.6	Semi-major axis computed from the analytical and the polyhedral propagation and their relative error.	31
4.7	Eccentricity computed from the analytical and the polyhedral propagation and their relative error.	31
4.8	Inclination computed from the analytical and the polyhedral propagation and their relative error.	32
4.9	Pericenter argument computed from the analytical and the polyhedral propagation and their relative error.	32
4.10	Right ascensions of the ascending node computed from the analytical and the poly- hedral propagation and their relative error.	32
4.11	True anomaly computed from the analytical and the polyhedral propagation and their relative error.	32
4.12	Initial two body problem orbit for the ManLab validation.	34
4.13	Two body problem ManLab continuation.	35
4.14	Evolution on the complex plane of the Floquet multipliers during the continuation of the solution branch.	35
4.15	Semi-major axis computed from ManLab and time integration and their relative error.	36
4.16	Eccentricity computed from ManLab and time integration and their relative error. .	36
4.17	Inclination computed from ManLab and time integration and their relative error. . .	36

4.18	Right ascension of the ascending node computed from ManLab and time integration and their relative error.	36
4.19	Pericenter argument computed from ManLab and time integration and their relative error.	37
5.1	L1 family computed through ManLab accounting 30 harmonics.	39
5.2	Jacobi constant vs orbit frequency along the continuation.	39
5.3	Evolution on the complex plane of the Floquet multipliers during the continuation of the L1 family.	40
5.4	L1 family computed through ManLab accounting for 200 harmonics.	40
5.5	Jacobi constant vs orbit frequency along the continuation.	40
5.6	H1 family computed through ManLab accounting 30 harmonics.	41
5.7	Jacobi constant vs orbit frequency along the continuation.	41
5.8	Evolution on the complex plane of the Floquet multipliers during the continuation of the H1 family.	41
5.9	H1 family computed through ManLab accounting for 200 harmonics.	42
5.10	Jacobi constant vs orbit frequency along the continuation.	42
5.11	A1 family computed through ManLab accounting 30 harmonics.	42
5.12	Jacobi constant vs orbit frequency along the continuation.	42
5.13	Evolution on the complex plane of the Floquet multipliers during the continuation of the A1 family.	43
5.14	V1 family computed through ManLab accounting 30 harmonics.	43
5.15	Jacobi constant vs orbit frequency along the continuation.	43
5.16	Evolution on the complex plane of the Floquet multipliers during the continuation of the V1 family.	44
5.17	Connection between the different family branches around the first Lagrange point.	44
5.18	Icosphere mesh and starting periodic orbit.	47
5.19	Icosphere orbit family computed through ManLab.	48
5.20	Jacobi constant vs orbit frequency along the continuation.	48
5.21	Evolution on the complex plane of the Floquet multipliers.	48
5.22	Trajectory x component computed through time integration and through ManLab.	49
5.23	Percentage relative error on the x component between the two methods.	49
5.24	Trajectory y component computed through time integration and through ManLab.	49
5.25	Percentage relative error on the y component between the two methods.	49
5.26	Trajectory z component computed through time integration and through ManLab.	50
5.27	Percentage relative error on the z component between the two methods.	50
5.28	Trajectory x component computed through HBM and through ManLab.	50
5.29	Percentage relative error on the x component between the two methods.	50
5.30	Trajectory y component computed through HBM and through ManLab.	51
5.31	Percentage relative error on the y component between the two methods.	51
5.32	Trajectory z component computed through HBM and through ManLab.	51
5.33	Percentage relative error on the z component between the two methods.	51
5.34	Icosphere orbit family computed through ManLab.	52
5.35	Jacobi constant vs orbit frequency along the continuation.	52
A.1	L2 family computed through ManLab accounting 200 harmonics.	V
A.2	H2 family computed through ManLab accounting 200 harmonics.	V

A.3	A2 family computed through ManLab accounting 200 harmonics.	V
A.4	V2 family computed through ManLab accounting 200 harmonics.	V
A.5	Connection between the different family branches around the second Lagrange point.	VI
A.6	L2 family computed through ManLab accounting 200 harmonics.	VI
A.7	H3 family computed through ManLab accounting 200 harmonics.	VI
A.8	A3 family computed through ManLab accounting 250 harmonics.	VII
A.9	V3 family computed through ManLab accounting 200 harmonics.	VII
A.10	Connection between the different family branches around the third Lagrange point.	VII

List of Tables

2.1	Equilibrium points coordinates and respective Jacobi constant of Earth-Moon system.	5
2.2	Equilibrium points and Jacobi constant of <i>1996 Hw1</i> .	7
2.3	Gravitational models advantages and drawbacks.	8
4.1	Two body problem validation orbit initial keplerain elements.	31
4.2	Reference and computed equilibrium points of <i>1996 Hw1</i> and their absolute error.	33
4.3	Reference and computed equilibrium points of <i>4769 Castalia</i> and their absolute error.	33
4.4	Reference and computed equilibrium points of <i>6489 Golevka</i> and their absolute error.	33
4.5	Initial two body problem orbit for the ManLab validation.	35
5.1	Necessary auxiliary variables for asteroid meshes.	47

Acronyms

ANM	Asymptotic Numerical Method
CR3BP	Circular Restricted Three Body Problem
CNSA	China National Space Administration
ESA	European Space Agency
HBM	Harmonic Balance Method
ICE	International Cometary Explorer
JAXA	Japan Aerospace eXploration Agency
NASA	National Aeronautics and Space Administration
NEAR	Near Earth Asteroid Rendezvous
NEAs	Near-Earth Asteroids
NEOs	Near-Earth Objects
SRP	Solar Radiation Pressure
3BP	Three Body Problem
USSR	Union of Soviet Socialist Republics
YORP	Yarkovsky-O'Keefe-Radzievskii-Paddack
ZVC	Zero Velocity Curves
ISS	International Space Station

Introduction

Since the beginning of the space age, targeting asteroids and comets has long captivated the attention of the engineering community. These missions are not only of cardinal importance in order to discover the origin and evolution of our Solar System but also hold the key to the future of space exploration. In recent times, they have gained notable relevance as crucial for planetary protection purposes. Moreover, these bodies possess abundant reserves of precious resources, which in the future could be exploited through mining missions, potentially leading to self-sustaining, long-duration space expeditions. As a result, international endeavors have been underway since the 80s to meticulously investigate these minor bodies.

1.1 Motivation and thesis outline

Initially, only missions that had accomplished or were on their way to reach their primary goals were sent toward asteroids and comets. In particular, the **NASA/ESA**'s mission *International Cometary Explorer (ICE)* was the first spacecraft to ever pass by a comet in 1985, crossing the tail of the *21P/Giacobini-Zinner* comet [1]. This was just the first of many future milestones. The following year, **USSR**'s missions *Vega 1* and *Vega 2* passed by the *Halley Comet* [2]. They paved the path which allowed *Giotto*, the first **ESA** deep space mission, to accomplish the first close flyby to the *Halley Comet* nucleus, coming as close as 600 km to it [3].

Before reaching the next important milestone, namely having the first man-made object to visit an asteroid, a few years had to pass. In 1991 and in 1993, while on its way to reach the Jovian system, **ESA**'s mission *Galileo* intercepted the asteroids *951 Gaspra* and *243 Ida*, discovering the first moon of an asteroid in the process [4]. The first mission to have an asteroid as primary target was **NASA**'s *Near Earth Asteroid Rendezvous (NEAR) Shoemaker*, targeting *433 Eros*. It achieved two groundbreaking milestones, by not only being the first spacecraft, in the year 2000, to ever orbit an asteroid, but also being the first to ever land on one's surface in 2001 [5].

Following this unprecedented fulfillment, the efforts shifted from simple orbiting and flyby missions to complex missions having the ambitious goal of landing and returning samples from the surface of these bodies.

The first one of this kind is **JAXA**'s *Hayabusa*, which in 2005 was capable of returning samples from *25143 Itokawa* [6]; the following year, **NASA**'s mission *Stardust* returned the first cometary sample, taken from the *81-P Wild* comet [7]. **ESA**'s mission *Rosetta* was the first spacecraft to orbit a cometary nucleus - *67P/Churyumov-Gerasimenko* -, and later, in 2014, the first to visit the surface thanks to a lander [8].

Most recent missions were targeting Near-Earth Asteroids (**NEAs**) in order to collect and return samples to Earth. In 2020 **JAXA**'s mission *Hayabusa 2* successfully returned samples from the asteroid *162173 Ryugu* [9], and **NASA**'s *OSIRIS-REx*, which landed on *101955 Bennu*, is expected to return samples in 2023 [10].

The first mission that could be classified as for planetary defense is **NASA**'s *Deep impact*, which in 2005 became the first spacecraft to ever collide with a comet [11]. However, the interest in these scopes drastically increased when a good opportunity to scale them up was found in binary asteroids. The joint **ESA**'s and **NASA**'s mission *AIDA* is aiming to assess the deflection of the secondary

body in the *65803 Didymos* system as a consequence of the kinetic impact carried out in 2022 with NASA's half of the mission: *DART* [12]. The results will be further assessed by ESA's part of the mission - *HERA* - scheduled to depart in 2024 [13].

Finally, several missions are already ongoing or are planned to be launched in the upcoming years. Near the end of 2021, NASA's mission *Lucy* has been launched and will explore the Trojan asteroids [14]. NASA's mission *Psyche* is scheduled to be launched at the end of 2023, after one year delay, in order to study the asteroid *16 Psyche*, which will be the first metallic asteroid to be explored [15]. CNSA's mission *Zheng He* is planned for launch in 2024, with the main goal to collect and return samples from the asteroid *69219 Kamo'oalewa* [16]. NASA's *NEO Surveyor*, will be sent in 2027 to seek out Near-Earth Objects (NEOs) [17]. JAXA's *Destiny +*, a technology demonstrator mission for the collection of dust from the asteroid *3200 Phaethon*, is scheduled for launch in 2028 [18]. Lastly, ESA's mission *Comet Interceptor*, with the revolutionary goal of flying past a comet at its first approach with the sun, will be launched in 2029 [19].

The computation of periodic orbits in non-Keplerian astrodynamical systems was already a topic of great interest due to their practical application in the Circular Restricted Three Body Problem (CR3BP), and due to the seen exponential increase of interest in missions around asteroids, the topic is acquiring a new wave of interest. However, due to the highly asymmetrical nature of these bodies, traditional time domain methods can be quite slow and heavy. In order to achieve a faster and easier resolution of the problem, Leclère [20] faced it with a frequency domain method: the well-known Harmonic Balance Method (HBM).

In this thesis, the problem is approached through a particular implementation of the method, implemented in the ManLab software. The software, is written to be faster and more efficient than the classical HBM.

Finally, frequency domain methods have the advantage over time domain methods not only for their velocity but also for their ability to better uncover the bifurcation dynamics of the system.

The aim of the thesis is to use ManLab in order to compute periodic orbits and analyze their bifurcations in the CR3BP and asteroid problem environments. Furthermore, the results will be used to assess the validity of the HBM implemented by Leclère.

For this purpose, the thesis is organized as follows:

- **Chapter 2** presents the state of the art regarding the circular restricted three-body problem and the problem of the motion around irregular-shaped bodies, emphasizing the issue in generating periodic orbits in such environments;
- **Chapter 3** enumerates the fundamentals and theory regarding the software used in order to generate families of orbits, including some elementary examples;
- **Chapter 4** reports the validation of the selected method for the computation of the gravitational potential, as well as of the software, through the application of the two-body problem;
- **Chapter 5** shows the application to the CR3BP and to the asteroid problem.

Theoretical background

This chapter provides an overview of the background needed to comprehend at best the topics presented in this thesis. It will first introduce two non-Keplerian problems: the circular restricted three-body problem and the problem of a particle around an irregular-shaped rotating body. Introducing for the latter different methods for the computation of the gravitational potential. The chapter will then focus on the techniques used for the generation of periodic orbits, providing a summary of the traditional techniques and those used within this thesis. The chapter ends with the introduction of the methods for the computation and analysis of the orbits' stability.

2.1 Circular restricted three-body problem

The **CR3BP** is the most widely used particular case to model the Three-Body Problem (**3BP**), as it represents one of its most accurate approximations. It describes the motion of a small body whose dynamics is driven by the attraction given by two principal bodies, with reference to which it is considered to be massless. These bodies are assumed to rotate around a common center of mass at a constant rate. **FIG. 2.1** shows the representation of the system in the rotating reference frame. Following the standard convention, the parameters and the equations of motion of the system are dimensionless.

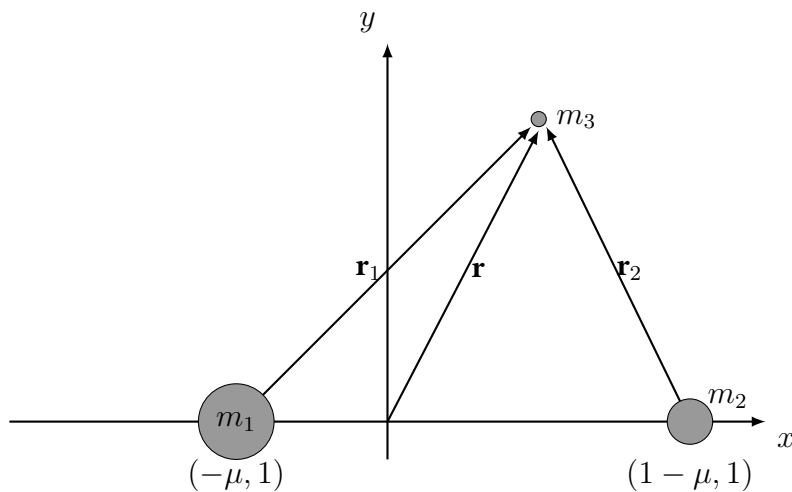


FIG. 2.1: Circular restricted three-body problem system in the rotating reference frame.

μ is a non-dimensional parameter depending only on the two main masses:

$$\mu = \frac{m_2}{m_1 + m_2}. \quad (2.1)$$

With these assumptions, it is possible to write the equations of motions of the third body as:

$$\begin{cases} \ddot{x} = x + 2\dot{y} - \frac{1-\mu}{r_1^3}(x + \mu) - \frac{\mu}{r_2^3}(x - 1 + \mu) \\ \ddot{y} = y - 2\dot{x} - \frac{1-\mu}{r_1^3}y - \frac{\mu}{r_2^3}y \\ \ddot{z} = -\frac{1-\mu}{r_1^3}z - \frac{\mu}{r_2^3}z \end{cases}, \quad (2.2)$$

where r_1 and r_2 are the relative distances between the third body and two primary ones:

$$r_1 = \sqrt{(x + \mu)^2 + y^2 + z^2} \quad r_2 = \sqrt{[x - (1 - \mu)]^2 + y^2 + z^2}. \quad (2.3)$$

2.1.1 Equilibrium points and zero velocity curves

Useful parameters for the analysis of the dynamical system are the quantities that are conserved during the motion. In the case of the **CR3BP**, only one quantity is constant and it is represented by the Hamiltonian of the equation of motion,

$$J = 2(T - U), \quad (2.4)$$

which in literature is known as the Jacobi integral. In this expression, U is the pseudo-potential function and T the kinetic energy, respectively computed as

$$U(x, y, z) = \frac{x^2 + y^2}{2} + \frac{1 - \mu}{r_1} + \frac{\mu}{r_2} + \mu \frac{1 - \mu}{2}; \quad T = \frac{1}{2}(\dot{x}^2 + \dot{y}^2 + \dot{z}^2). \quad (2.5)$$

As the Jacobi integral is constant during the motion of the particle, it is defined only by the initial conditions and can be used to define the Jacobi constant C, where

$$J + C = 0. \quad (2.6)$$

This constant describes the relative energy of the particle that is still available for its motion. Exploiting this definition, it is possible to define the so-called zero velocity curves (**ZVC**), by considering the case in which the kinetic energy is zero:

$$C = 2U. \quad (2.7)$$

This provides information regarding the possibility for the particle to move in a certain region of space: different levels of relative energy correspond to different accessible portions of space. In fact, the inequality

$$C > 2U \quad (2.8)$$

denotes the forbidden regions which cannot be accessed by the particle, as it does not have enough energy to reach them. On the contrary, the inequality

$$C \leq 2U \quad (2.9)$$

denotes regions the particle is able to reach.

Finally, it is important to define the equilibrium points, i.e. particular orbits that remain static in the rotating frame and which are characterized by a zero acceleration and velocity of the particle. These points can be computed by setting the quantities in **Eq. 2.2** to zero. The **CR3BP** has five potential equilibrium points, also known as Lagrangian points, out of which two are stable while

the remaining three are not.

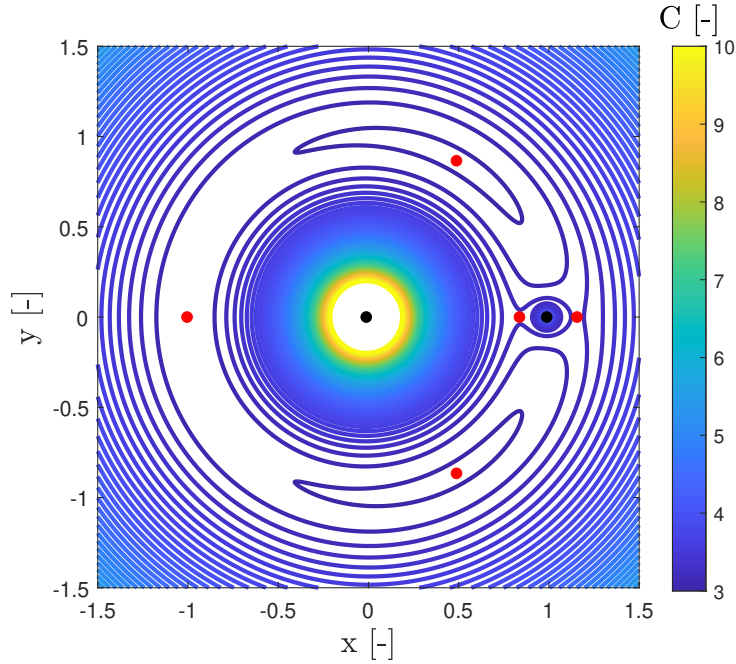


FIG. 2.2: ZVC and equilibrium points of Earth-Moon system.

TAB. 2.1 Equilibrium points coordinates and respective Jacobi constant of Earth-Moon system.

Equilibrium point	x [-]	y [-]	z [-]	C [-]
1	0.8369	0	0	3.2003
2	1.1557	0	0	3.1842
3	-1.0051	0	0	3.0241
4	0.4878	0.8660	0	3.0000
5	0.4878	-0.8660	0	3.5000

FIG. 2.2 shows the computed ZVC for the Earth-Moon system in which $\mu = 0.01215$, and **TAB. 2.1** lists the coordinates of its Lagrangian points along with their Jacobi constant.

2.2 Asteroid case

Asteroids are irregular-shaped bodies with a quite fast period of rotation. Therefore, the classical two-body problem equation of motions are not well suited in order to adequately describe the problem. Instead, due to its rotating nature, it resembles the dynamics of the **CR3BP**.

The dynamics of a massless particle in a rotating frame attached to the asteroid can be described by the following equation of motion

$$\ddot{\mathbf{r}} + 2\boldsymbol{\Omega} \times \dot{\mathbf{r}} + \boldsymbol{\Omega} \times (\boldsymbol{\Omega} \times \mathbf{r}) + \dot{\boldsymbol{\Omega}} \times \mathbf{r} = \nabla U(\mathbf{r}) \quad (2.10)$$

where \mathbf{r} is the position vector, $\boldsymbol{\Omega}$ is the asteroid's angular velocity vector having magnitude $|\boldsymbol{\Omega}| = \omega_a$ and $\nabla U(\mathbf{r})$ is the gradient of the gravitational potential $U(\mathbf{r})$ [21].

In general, the variation of the angular velocity vector in time is non-zero, due to the so-called

YORP effect [22]. However, as the timescale of interest for spacecraft mission design is typically contained with respect to the timescale needed to have significant variations in the angular velocity vector, this variation can be neglected in the first approximation, leading the equation of motion to be written as

$$\ddot{\mathbf{r}} + 2\boldsymbol{\Omega} \times \dot{\mathbf{r}} + \boldsymbol{\Omega} \times (\boldsymbol{\Omega} \times \mathbf{r}) = \nabla U(\mathbf{r}). \quad (2.11)$$

For simplicity it is assumed that $\boldsymbol{\Omega} = \omega_a \hat{\mathbf{k}}$.

2.2.1 Equilibrium points and zero velocity curves

As for the previous problem, it is necessary to find quantities that are constant during the motion. With the hypothesis of uniform angular velocity, once again only the Hamiltonian of the system is conserved, and also in this case it is known as Jacobi integral as it represents the same physical concept seen before

$$J = \frac{1}{2} \dot{\mathbf{r}} \cdot \dot{\mathbf{r}} - \frac{1}{2} (\boldsymbol{\Omega} \times \mathbf{r}) \cdot (\boldsymbol{\Omega} \times \mathbf{r}) - U(\mathbf{r}). \quad (2.12)$$

Eq. 2.12 is divided into kinetic energy and effective potential which represent the combination of the gravitational and centrifugal potential energy, respectively defined as

$$T(\mathbf{r}) = \frac{1}{2} \dot{\mathbf{r}} \cdot \dot{\mathbf{r}} \quad (2.13)$$

$$V(\mathbf{r}) = \frac{1}{2} (\boldsymbol{\Omega} \times \mathbf{r}) \cdot (\boldsymbol{\Omega} \times \mathbf{r}) + U(\mathbf{r}). \quad (2.14)$$

As before the Jacobi constant is an extremely useful quantity and can be defined from the Jacobi integral as

$$J + C = 0 \quad (2.15)$$

and therefore, in combination with the definition of the effective potential showed in **Eq.** 2.14, the Jacobi constant can be computed as

$$C = V(\mathbf{r}) - T(\mathbf{r}). \quad (2.16)$$

By exploiting its definition, it is possible to define **ZVC** also for this system

$$C = V(\mathbf{r}). \quad (2.17)$$

This equation points out non accessible regions of space if

$$C > V(\mathbf{r}), \quad (2.18)$$

and accessible ones if

$$C \leq V(\mathbf{r}). \quad (2.19)$$

Finally, according to [23], equilibrium points must satisfy the condition

$$\nabla V(\mathbf{r}) = 0. \quad (2.20)$$

Therefore, every combination of shape and angular velocity leads to different equilibrium points, showing the importance to define these quantities as accurate as possible. In general, the number of equilibrium points is not known a priori and heavily depends on the shape of the body. Moreover, one or more points can fall inside it.

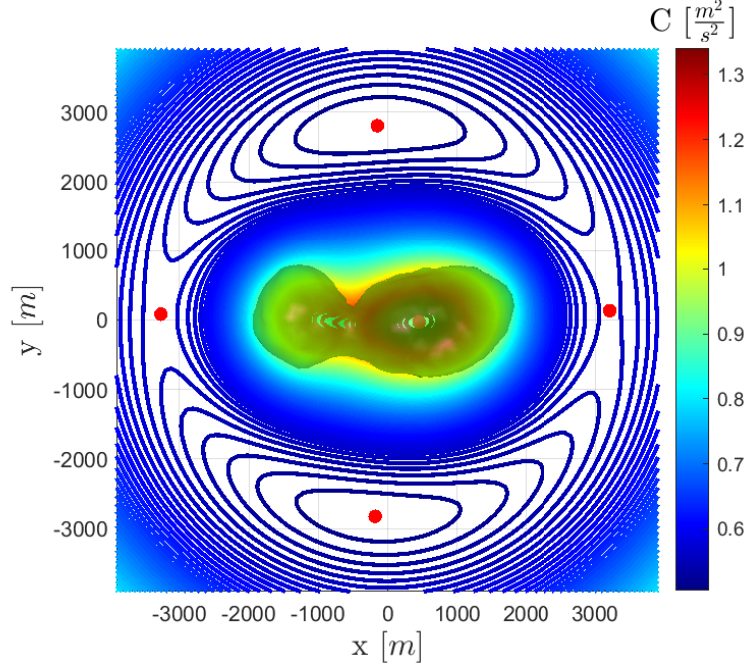


FIG. 2.3: ZVC and equilibrium points of 1996 Hw1.

TABLE 2.2 Equilibrium points and Jacobi constant of 1996 Hw1.

Equilibrium point	x [m]	y [m]	z [m]	C [m ² /s ²]
1	-150.18	2807.9	0.25	0.505
2	3212	134.25	-2.64	0.554
3	-181.05	-2826	0.0586	0.5068
4	-3286.6	84.467	-1.347	0.5598
5	452.6	29.1	2.9	1.3389

FIG. 2.3 displays the ZVC for a quite irregular asteroid and it clearly shows the presence of five equilibrium points, one of which is inside the body. TABLE 2.2 gives the coordinates and the Jacobi constant of these points.

2.2.2 Gravitational potential

In the surroundings of an asteroid, due to its highly rough shape, the gravitational field is highly irregular and in proximity to the surface it completely drives the interesting dynamics, making external disturbances such as solar radiation pressure (SRP) negligible [24]. In order to design reliable missions it is extremely important to accurately model the dynamical environment. Therefore, throughout years a great deal of effort has been put in order to refine the available gravitational models.

The first step towards a better understanding of the dynamical behavior around complex shape bodies was made through analytical models based on regular body shapes. These models were recently used to study periodic orbits, such as a solid circular ring [25], a homogeneous annulus disk [26], a homogeneous cube [27], a dumbbell [28], a straight segment [29] and a particle-linkage [30].

Only in 1958 one of the most efficient models based on triaxial ellipsoid was developed in closed form [31] and later in 1978 in approximated form with spherical harmonics expansion [32]. However, these models had divergence problems. These problems were solved in 1996 when the constant density polyhedron model was developed [33] and lastly with the mass concentration model (mascon) which accounts for the internal density distribution [34].

TAB. 2.3 summarizes the most important advantages and drawbacks of the currently used gravitational models, which together with a general overview, can be used to justify the choices made for this work.

TAB. 2.3 Gravitational models advantages and drawbacks.

Model	Advantages	Drawbacks
Spherical Harmonic Expansion	<ul style="list-style-type: none"> - Tends to exact gravity increasing the order - Low computational cost - Weakly affected by accuracy level 	<ul style="list-style-type: none"> - Valid only outside of the Brillouin sphere
Constant Density Ellipsoid	<ul style="list-style-type: none"> - Simple implementation - Good first approximation 	<ul style="list-style-type: none"> - Far from the actual field in surface proximity
Constant Density Polyhedron	<ul style="list-style-type: none"> - Deals with any shape - Exact gravity field for the given shape - Gravity field up to the body's surface - Laplacian to check the field point position 	<ul style="list-style-type: none"> - Density must be constant - High computational cost
Mass Concentration	<ul style="list-style-type: none"> - Deals with any shape and density variation - Deals with non-homogeneous bodies - Valid up to the body's surface 	<ul style="list-style-type: none"> - No method for checking field point position - High computational cost - Less accurate than harmonic expansion

Spherical Harmonics Expansion

By constructing a set of orthogonal solutions to Laplace's equation and choosing the coefficients of the expansion to match with the actual potential function it is possible to model the gravitational potential.

In particular, Laplace's equation is solved by a separation of variables in terms of spherical coordinates [22], leading to

$$U(r, \delta, \lambda) = \frac{\mu}{r} \sum_{l=0}^{\infty} \sum_{m=0}^l \left(\frac{r_o}{r}\right)^l P_{lm}(\sin \delta) [C_{lm} \cos m\lambda + S_{lm} \sin m\lambda] \quad (2.21)$$

where δ is the latitude, λ is the longitude, $\mu = GM$ is the body gravitational parameter, r_o is the normalizing radius which is often chosen as either the maximum radius or the mean radius of the body. P_{lm} are the associated Legendre functions and C_{lm} and S_{lm} are the gravity field harmonic coefficients, also known as Stokes coefficients.

However, this approach is not guaranteed to work in all situations. The spherical harmonic expansion in **EQ.** 2.21 cannot be used when considering the gravitational potential close to an irregular-shaped small body. In fact, the divergence is severe within the circumscribing sphere of the body shown in **FIG.** 2.4, also known as Brillouin sphere, making the gravitational potential worthless for dynamical computation in this region.

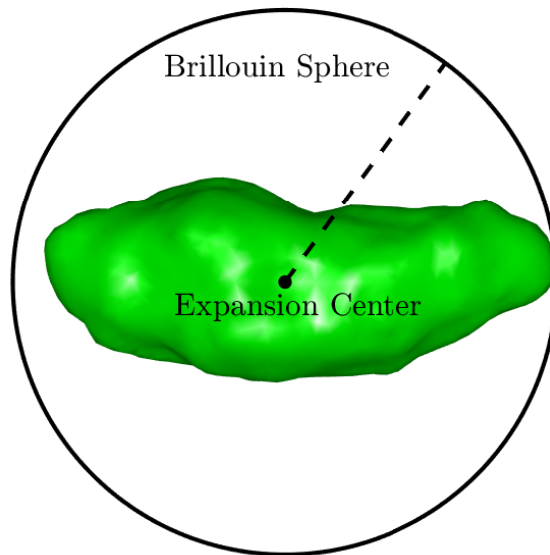


FIG. 2.4: Brillouin sphere of asteroid *1620 Geographos*.

Constant Density Ellipsoid

We now consider the ellipsoid shown in **FIG.** 2.5. It has semi-major axes $\alpha \geq \beta \geq \gamma$

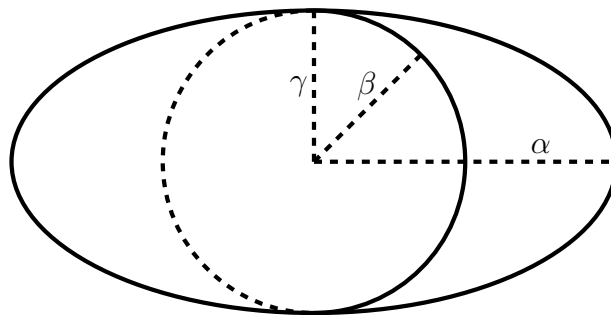


FIG. 2.5: Tri-axial ellipsoid.

and it is mathematically defined as

$$\left(\frac{x}{\alpha}\right)^2 + \left(\frac{y}{\beta}\right)^2 + \left(\frac{z}{\gamma}\right)^2 \leq 1 \quad (2.22)$$

Assuming homogeneous density ρ , it is possible to compute the exterior gravitational potential at the point \mathbf{r} in closed form [35] as follows

$$\begin{aligned}
U(\mathbf{r}) = & -\frac{3\mu}{2\sqrt{\alpha^2 - \gamma^2}} \left\{ \left[1 - \frac{x^2}{\alpha^2 - \beta^2} + \frac{y^2}{\alpha^2 - \beta^2} \right] F(\phi_k, k) + \right. \\
& + \left[\frac{x^2}{\alpha^2 - \beta^2} - \frac{(\alpha^2 - \gamma^2)y^2}{(\alpha^2 - \beta^2)(\beta^2 - \gamma^2)} + \frac{z^2}{\beta^2 - \gamma^2} \right] E(\phi_k, k) + \\
& \left. + [(\gamma^2 + k)y^2 - (\beta^2 + k)z^2] \frac{\sqrt{\alpha^2 - \gamma^2}}{(\beta^2 - \gamma^2)\Delta(k)} \right\}. \quad (2.23)
\end{aligned}$$

In **EQ. 2.23** $\mu = \frac{4}{3}G\rho\pi\alpha\beta\gamma$ is the gravitational parameter of the ellipsoid, $F(\phi_k, k)$ and $E(\phi_k, k)$ are the elliptic integrals of the first and second kind, respectively, and k is the largest root of **EQ. 2.24**, which always exist.

$$\frac{x^2}{\alpha^2 + k} + \frac{y^2}{\beta^2 + k} + \frac{z^2}{\gamma^2 + k} = 1 \quad (2.24)$$

and also

$$\Delta(k) = \sqrt{(\alpha^2 + k) + (\beta^2 + k) + (\gamma^2 + k)}, \quad (2.25)$$

$$k = \frac{\alpha^2 - \beta^2}{\alpha^2 - \gamma^2}, \quad \phi_k = \sin^{-1} \sqrt{\frac{\alpha^2 - \gamma^2}{\alpha^2 + k}}. \quad (2.26)$$

The model is quite simple, however, if the shape of the asteroid under study is too far from the ellipsoid shape and the analysis is carried in proximity of the surface, the committed error would be too large.

Constant Density Polyhedron

The method is based on two main hypotheses: the asteroid is a polyhedron, and the polyhedron's density is constant.

A polyhedron is understood to be a three-dimensional solid body whose surface consists of planar faces meeting along straight edges or at isolated points called vertices. Exactly two faces meet at each edge. Three or more edges and a like number of faces meet at each vertex. As the vertex coordinates are insufficient to describe a polyhedron, the connective topology must also be described, edges connect which vertex pairs and bound which face pairs [33].

After the mathematical manipulations, well described in [33], the following expressions to precisely model the potential U in the field-point location \mathbf{r} can be derived:

$$U(\mathbf{r}) = \frac{1}{2}G\sigma \sum_{e \in \text{edges}} \mathbf{r}_e \cdot \mathbf{E}_e \cdot \mathbf{r}_e L_e - \frac{1}{2}G\sigma \sum_{f \in \text{faces}} \mathbf{r}_f \cdot \mathbf{F}_f \cdot \mathbf{r}_f \omega_f \quad (2.27)$$

$$\nabla U(\mathbf{r}) = -G\sigma \sum_{e \in \text{edges}} \mathbf{E}_e \cdot \mathbf{r}_e L_e + G\sigma \sum_{f \in \text{faces}} \mathbf{F}_f \cdot \mathbf{r}_f \omega_f \quad (2.28)$$

$$\nabla \nabla U(\mathbf{r}) = G\sigma \sum_{e \in \text{edges}} \mathbf{E}_e L_e - G\sigma \sum_{f \in \text{faces}} \mathbf{F}_f \omega_f \quad (2.29)$$

$$\nabla^2 U(\mathbf{r}) = -G\sigma \sum_{f \in \text{faces}} \omega_f. \quad (2.30)$$

\mathbf{r}_f is the vector from the field-point location to a point belonging to the face f and \mathbf{r}_e is the vector from the field-point location to a point belonging to the edge e .

Symbols G and σ represent the gravitational constant and the polyhedron's density. Suffices e and f indicate edge and face, respectively. Each polyhedron face has an outward-pointing face normal vector $\hat{\mathbf{n}}_f$ and a face dyad $\mathbf{F}_f = \hat{\mathbf{n}}_f \hat{\mathbf{n}}_f$. Each edge of each face exhibits an outward-pointing edge normal vector $\hat{\mathbf{n}}_e^f$ perpendicular to both $\hat{\mathbf{n}}_f$ and the edge. **FIG. 2.6** shows the edge and the faces connecting vertices P_1 and P_2 . In this case, the edge dyad is $\mathbf{E}_{12} = \hat{\mathbf{n}}_A \hat{\mathbf{n}}_{12}^A + \hat{\mathbf{n}}_B \hat{\mathbf{n}}_{21}^B$, while the faces dyad are $\mathbf{F}_1 = \hat{\mathbf{n}}_A \hat{\mathbf{n}}_A$ and $\mathbf{F}_2 = \hat{\mathbf{n}}_B \hat{\mathbf{n}}_B$.

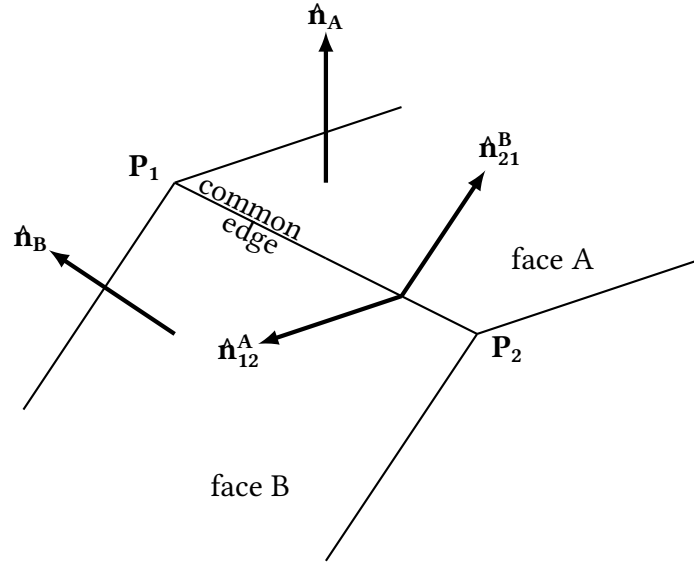


FIG. 2.6: Schematic of two faces with a common edge and their respective normal [33].

Let \mathbf{r}_i represent the vector from the variable field-point location to polyhedron vertex P_i , and let $r_i = \|\mathbf{r}_i\|$ be its length. For the polyhedron edge connecting vertices P_i and P_j of constant length e_{ij} , the dimensionless per-edge factor L_e is

$$L_e = \ln \frac{r_i + r_j + e_{ij}}{r_i + r_j - e_{ij}}. \quad (2.31)$$

For a triangular face f bounded by vertices P_i, P_j, P_k , the dimensionless per-face factor ω_f is

$$\omega_f = 2 \arctan \frac{\mathbf{r}_i \cdot \mathbf{r}_j \times \mathbf{r}_k}{r_i r_j r_k + r_i (\mathbf{r}_j \cdot \mathbf{r}_k) + r_j (\mathbf{r}_k \cdot \mathbf{r}_i) + r_k (\mathbf{r}_i \cdot \mathbf{r}_j)}. \quad (2.32)$$

The polyhedron method comes with many advantages:

- The gravity field is exact for the given shape and density. Errors can be reduced entirely to errors in the asteroid shape determination and the level of discretization chosen. Since most asteroid shape determinations have limited shape resolution, this approach provides gravitational accuracy consistent with the accuracy of the shape determination.
- Polyhedron gravitation is a valid and exact solution up to the surface of the body.
- The Laplacian $\nabla^2 U(\mathbf{r})$ is an extremely interesting value, it is useful to determine whether or not the particle is inside the polyhedron model or not. The sum $\sum \omega_f$ vanishes when the field point is outside the polyhedron, and equals -4π inside.

- Any body of arbitrary shape can be approximated with a polyhedron having a variable number of triangular faces.

The polyhedron meshes are mostly provided by NASA and collected in catalogs such as [36], an example is shown in FIG. 2.7. In general, these meshes have been created exploiting three main methods: spacecraft imaging, radar imaging and lightcurve inversion.

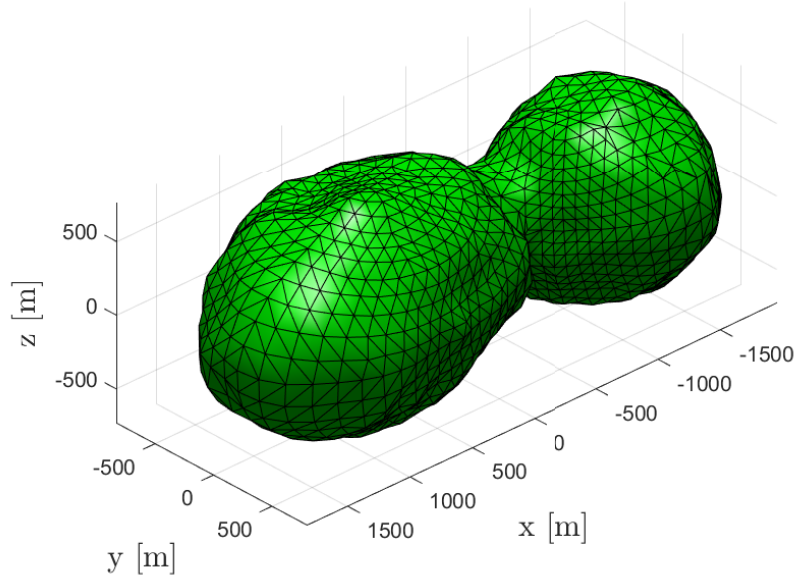


FIG. 2.7: Polyhedron mesh of the asteroid *1996 Hw1*.

Mass Concentration

Conceptually, the so-called mascons approach is one of the simplest model, it uses various point masses in order to model the body's mass distribution.

Assuming the asteroid is a polyhedron, it is possible to fill its interior with non-overlapping spheres which cover the entire volume. These spheres are assigned with a particular mass density and can be of various or of the same size, with the second option requiring more spheres and therefore increasing the computation time.

The potential of a body modeled with N mascons is computed as follows [37]

$$U(\mathbf{r}) = -\mu \sum_{i=1}^N \frac{m'_i}{|\mathbf{r} - \mathbf{r}_i|} \quad (2.33)$$

in which \mathbf{r}_i is the position of the point mass with mass m_i and

$$m'_i = \frac{m_i}{m} \quad m = \sum_{i=1}^N m_i. \quad (2.34)$$

An important advantage of the method is that it is capable of modeling the potential of non-homogeneous bodies up to their surface by using a suitable distribution of mass values to each

sphere, however it does not provide any information to understand if the field point is inside the body. For a given computational effort it is less accurate than the harmonic approach.

In conclusion, in the framework of this thesis was chosen to use the constant density polyhedron model, as it is comparatively simple to implement, it provides an accurate model of the gravitational potential in close form both near and far from the body's surface, and finally, because it can be relatively easily recast in quadratic form as will be shown in Section 5.2.1. This will prove an important requirement.

2.3 Periodic orbit generation

One of the crucial aspects when dealing with non-Keplerian motion is the ability to generate periodic orbits. In general, numerical methods are the most powerful tool available for the scope. They implement three fundamental steps in order to achieve such objective, schematically summarised in **FIG. 2.8**. The starting point is to generate initial guesses through the use of generation algorithms, which need to be processed by correction algorithms in order to converge to the targeted solution. This is necessary because the dynamic is strongly non-linear and a small variation in the initial conditions can lead to very different trajectories. Finally, continuation techniques can provide new initial guesses starting from the information available on other members of the family.

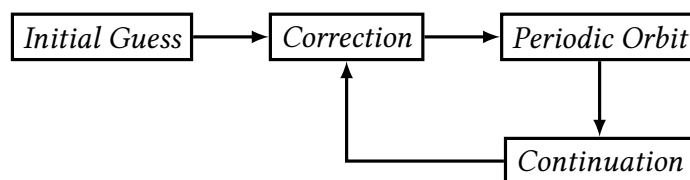


FIG. 2.8: General periodic orbit generation scheme

As well reported in [38], for every step of the scheme various traditional solutions are available and used within the literature.

Initial Guess

The fastest and easiest way to find an initial guess is to consult a catalogue of periodic solutions such as [39]. However, catalogues are not yet available for many cases. For all the cases where the catalogues are not available, a very effective strategy is the use of Poincaré maps. They are defined as the set of points which intersects the hyperplane Σ , transversal to the n -dimensional flow ϕ of the dynamical system. Periodic orbits are represented on the map as fixed points. The method had been extensively used for many studies until computational power was sufficient to afford the use of grid searching methods [40]. Combined with a hierarchical parametrization, they gave rise to the well-known and highly used hierarchical grid search method [41].

Correction

The most widely used technique for numerical correction is based on the differential correction algorithm built on the one proposed by Howell [42]. These methods rely on constraints, typically one of them is periodicity to ensure that the initial conditions repeat themselves after an amount of time, and based on free variables as well, which could be modified by the corrector.

In astrodynamics applications, there are two common differential correction implementations, single and multiple shooting. In the case of single-shooting, the initial state is integrated into a single arc and the trajectory is found whenever it returns at its initial state. By contrast, in the multiple-shooting case, the initial guess trajectory is discretized in patch points, which are independently integrated so that the complete solution is made by multiple arcs. In this case, the constraints do not only include periodicity but continuity as well.

An alternative to differential correction is the use of optimization algorithms as finding periodic solutions can be seen as solving a boundary value problem.

Continuation

There exist different continuation approaches, among them the so-called single or multiple parameter continuation, consisting in the variation of one or multiple parameters in the initial condition. Typical parameters are the initial position, the energy or the period. Recently it evolved into the shape continuation method [37] in which the continuation parameter is the shape of the asteroid body.

Another method is a particular case of the multiple parameter continuation called pseudo-arclength continuation, generally being more robust and efficient. In this method, the continuation parameters are not chosen a priori, but the free variable vector is instead continued along the tangent direction to the targeted family.

In his work, Leclère [20], proposed an innovative way of facing the problem, the **HBM**. In contrary to the aforementioned classical methods, the **HBM** targets the problem in the frequency domain. Being part of the fundamentals of the software used in this thesis, it will be briefly explained in the following.

2.3.1 The Harmonic Balance Method

The method is very well known in the field of non-linear dynamics, typically used for non-linear vibrations and aerodynamics. It consists of the approximation of periodic signals with their Fourier coefficients, becoming the new unknowns of the problem.

The procedure behind the method is well explained in [43] and here summarised.

The general form of the equation of motions for a nonlinear dynamical system is

$$\mathbf{M}\ddot{\mathbf{x}} + \mathbf{C}\dot{\mathbf{x}} + \mathbf{K}\mathbf{x} + \mathbf{f}_{nl}(\mathbf{x}, \dot{\mathbf{x}}) = \mathbf{f}_{ext}(\omega, t) \quad (2.35)$$

in which \mathbf{M} , \mathbf{C} and \mathbf{K} are the mass, damping and stiffness matrix, respectively. Vectors f_{nl} and f_{ext} represent the nonlinear forces and the external forces, where the latter is supposed to be periodic with frequency ω .

In the particular case of **EQ. 2.11**, the system has three degrees of freedom, and as it is not excited, the vector of external forces $\mathbf{f}_{ext}(\omega, t) = 0$. The corresponding mass, damping, and stiffness matrices are

$$\mathbf{M} = \begin{bmatrix} 1 & 0 & 0 \\ 0 & 1 & 0 \\ 0 & 0 & 1 \end{bmatrix} \quad \mathbf{C} = \begin{bmatrix} 0 & -2\omega_a & 0 \\ 2\omega_a & 0 & 0 \\ 0 & 0 & 0 \end{bmatrix} \quad \mathbf{K} = \begin{bmatrix} -\omega_a^2 & 0 & 0 \\ 0 & -\omega_a^2 & 0 \\ 0 & 0 & 0 \end{bmatrix} \quad (2.36)$$

and the nonlinear forces term is $\mathbf{f}_{nl} = -\nabla U$.

As the solution of the equation of motion and the forcing term are assumed to be periodic, their signals are approximated by Fourier series truncated to the N_H -th harmonic:

$$\mathbf{x}(t) = \frac{c_0^x}{\sqrt{2}} + \sum_{k=1}^{N_H} s_k^x \sin(k\omega t) + c_k^x \cos(k\omega t) \quad (2.37)$$

$$\mathbf{f}(t) = \frac{c_0^f}{\sqrt{2}} + \sum_{k=1}^{N_H} s_k^f \sin(k\omega t) + c_k^f \cos(k\omega t) \quad (2.38)$$

where \mathbf{s}_k and \mathbf{c}_k represent the vectors of the Fourier coefficients related to the sine and cosine terms, respectively. The Fourier coefficients of $\mathbf{f}(t)$ depend on the Fourier coefficients of the displacement $\mathbf{x}(t)$ building the new unknown of the problem. These coefficients are collected into $(2N_H + 1)n \times 1$ vectors. \mathbf{z} for the displacement related and \mathbf{b} for the one associated to the force

$$\mathbf{z} = [(c_0^x)^T (s_1^x)^T (c_1^x)^T \dots (s_{N_H}^x)^T (c_{N_H}^x)^T] \quad (2.39)$$

$$\mathbf{b} = [(c_0^f)^T (s_1^f)^T (c_1^f)^T \dots (s_{N_H}^f)^T (c_{N_H}^f)^T] \quad (2.40)$$

Eq. 2.37 and **Eq. 2.38** are reduced to a compact form through the Kronecker tensor product (\otimes)

$$\mathbf{x}(t) = (\mathbf{Q}(t) \otimes \mathbb{I}_n) \mathbf{z} \quad (2.41)$$

$$\mathbf{f}(t) = (\mathbf{Q}(t) \otimes \mathbb{I}_n) \mathbf{b} \quad (2.42)$$

where \mathbb{I}_n is the identity matrix of size n and $\mathbf{Q}(t)$ is built as follows

$$\mathbf{Q}(t) = \left[\frac{1}{\sqrt{2}} \sin(\omega t) \cos(\omega t) \dots \sin(N_H \omega t) \cos(N_H \omega t) \right]. \quad (2.43)$$

The vectors of both velocities and accelerations are expressed using **Eq. 2.43**

$$\dot{\mathbf{x}}(t) = (\dot{\mathbf{Q}}(t) \otimes \mathbb{I}_n) \mathbf{z} = (\mathbf{Q}(t) \nabla \otimes \mathbb{I}_n) \mathbf{z} \quad (2.44)$$

and

$$\ddot{\mathbf{x}}(t) = (\ddot{\mathbf{Q}}(t) \otimes \mathbb{I}_n) \mathbf{z} = (\mathbf{Q}(t) \nabla^2 \otimes \mathbb{I}_n) \mathbf{z} \quad (2.45)$$

where

$$\nabla = \begin{bmatrix} 0 & & & & \\ & \ddots & & & \\ & & \nabla_k & & \\ & & & \ddots & \\ & & & & \nabla_{N_H} \end{bmatrix}, \quad \nabla^2 = \begin{bmatrix} 0 & & & & \\ & \ddots & & & \\ & & \nabla_k^2 & & \\ & & & \ddots & \\ & & & & \nabla_{N_H}^2 \end{bmatrix} \quad (2.46)$$

with

$$\nabla_k = \begin{bmatrix} 0 & -k\omega \\ k\omega & 0 \end{bmatrix}, \quad \nabla_k^2 = \begin{bmatrix} -(k\omega)^2 & 0 \\ 0 & -(k\omega)^2 \end{bmatrix}. \quad (2.47)$$

with

$$\mathbf{J}(\mathbf{y}_i) = [\mathbf{h}_z(\mathbf{y}_i) \quad \mathbf{h}_\omega(\mathbf{y}_i)], \quad (2.55)$$

where $\mathbf{h}_\omega = \partial \mathbf{h} / \partial \omega$. The last row in **EQ. 2.54** prevents the continuation from turning back and, for the first iteration is replaced by a line of ones. Doing so, the sum of the tangent's components is forced to be 1. The predictions of $\mathbf{y}_{(i+1)}^{(1)}$ are then built as

$$\mathbf{y}_{(i+1)}^{(1)} = \mathbf{y}_{(i)} + s_{(i)} \mathbf{t}_{(i)} \quad (2.56)$$

where $s_{(i)}$ is the predictor step size. Then the second stage uses Newton's method for the correction of the prediction.

2.4 Stability

The stability of the periodic solutions obtained through the HBM is assessed by means of the Floquet multipliers $\tilde{\sigma}$, or equivalently via the Floquet exponents $\tilde{\lambda}$, which are related through the exponential function

$$\tilde{\sigma}_i = e^{\tilde{\lambda}_i T}, \quad i = 1, \dots, 2n. \quad (2.57)$$

If there exist at least one Floquet multiplier with a magnitude higher than 1 or, through **EQ. 2.57**, at least one Floquet exponent with real part higher than 0, then the computed periodic solution is unstable. Otherwise, it is stable.

In general, the Floquet exponents and multipliers are depicted in the complex plane and compared to the unit circle or to the imaginary axis, respectively [44].

In the traditional time domain approach, the multipliers are obtained through the use of the monodromy matrix. While in frequency domain, a variety of methods are available, in this case, Hill's method was applied, as it is well adapted to work with the HBM.

The general idea of Hill's method is to introduce a periodic perturbation $\mathbf{s}(t)$ multiplied by an exponential decay to a periodic orbit $\mathbf{x}^*(t)$, as in **EQ. 2.58**:

$$\mathbf{p}(t) = \mathbf{x}^*(t) + e^{\lambda T} \mathbf{s}(t) \quad (2.58)$$

which fulfills **EQ. 2.11** [45].

This perturbed solution is then introduced in the equation of motion, obtaining

$$\mathbf{M}\ddot{\mathbf{x}}^* + \mathbf{C}\dot{\mathbf{x}}^* + \mathbf{K}\mathbf{x}^* + [\lambda^2 \mathbf{M}\mathbf{s} + \lambda(2\mathbf{M}\dot{\mathbf{s}} + \mathbf{C}\mathbf{s}) + \mathbf{M}\ddot{\mathbf{s}} + \mathbf{C}\dot{\mathbf{s}} + \mathbf{K}\mathbf{s}] e^{\lambda T} = \mathbf{f}(\mathbf{p}, \dot{\mathbf{p}}, \omega, t). \quad (2.59)$$

EQ. 2.59 can be solved similarly to the unperturbed one. First, both the periodic solution $\mathbf{x}^*(t)$ and the perturbation $\mathbf{s}(t)$ are approximated by Fourier series truncated at the N_H -th order. Second the Galerkin procedure is applied to obtain

$$\mathbf{A}\mathbf{z}^* + (\Delta_2 \lambda^2 + \Delta_1 \lambda + \mathbf{A}) e^{\lambda t} \mathbf{u} = \mathbf{b}(\mathbf{z}^* + e^{\lambda t} \mathbf{u}) \quad (2.60)$$

in which

$$\Delta_1 = \nabla \otimes 2\mathbf{M} + \mathbb{I}_{2N_H+1} \otimes \mathbf{C}, \quad \Delta_2 = \mathbb{I}_{2N_H+1} \otimes \mathbf{M}. \quad (2.61)$$

Thus, the right-hand side of this equation is evaluated through a Taylor series expansion around the solution \mathbf{z}^* :

$$\mathbf{b}(\mathbf{z}^* + e^{\lambda t} \mathbf{u}) = \mathbf{b}(\mathbf{z}^*) + \left. \frac{\partial \mathbf{b}}{\partial \mathbf{z}} \right|_{\mathbf{z}=\mathbf{z}^*} (e^{\lambda t} \mathbf{u}). \quad (2.62)$$

Given that $\mathbf{A}\mathbf{z}^* - \mathbf{b}(\mathbf{z}^*) = 0$ by definition and that $\mathbf{A} - \left. \frac{\partial \mathbf{b}}{\partial \mathbf{z}} \right|_{\mathbf{z}=\mathbf{z}^*} = \mathbf{h}_z$, replacing EQ. 2.62 in EQ. 2.60 leads to

$$(\Delta_2 \lambda^2 + \Delta_1 \lambda + \mathbf{h}_z) e^{\lambda t} \mathbf{u} = 0. \quad (2.63)$$

As a result, Hill's coefficients λ are the solutions of the quadratic eigenvalue problem:

$$(\Delta_2 \lambda^2 + \Delta_1 \lambda + \mathbf{h}_z) \mathbf{u} = 0. \quad (2.64)$$

Among the complete set of λ , only the $2n$ with the smallest imaginary part in modulus approximate the Floquet exponents $\tilde{\lambda}$ of the solution $\mathbf{x}^*(t)$ [46].

Due to the autonomous nature of the set of equations of motion, two Floquet exponents are null, this could affect the bifurcation detection. In order to solve the issue [47] proposed to shift twice the quadratic eigenvalue problem.

The obtained Floquet exponents, not only provide information about the stability of the periodic solution; they can also be used for the detection of bifurcations, particular points of the branch in which the stability of the system change. For periodic orbits around celestial bodies, four different types of bifurcations based on the Floquet theory can be classified [48]: tangent bifurcations, period-doubling bifurcations, real saddle bifurcations and Neimark-Sacker bifurcations.

Tangent bifurcations

A tangent bifurcation occurs when the orbit has characteristic multipliers that cross 1, and the motion of the characteristic multipliers causes them to leave the unit circle for the real axis, or contrarily from the real axis to the unit circle. There exist two types of tangent bifurcations; the fold bifurcation and the branchpoint. The former is characterized by the collision of two stable and unstable solutions, while the latter is identified by a change of stability followed by the creation of new branches. The uniqueness of the solution is lost and two types of branchpoints can occur. Either the curve of the solution loops back on itself, categorized as transcritical bifurcation, or the symmetry of the system is broken and a new branch, symmetric to the main one, is created.

Period-doubling bifurcations

This type of bifurcation occurs when the orbit has characteristic multipliers that cross -1 , and the motion of the characteristic multipliers causes them to leave the unit circle for the real axis, or contrarily from the real axis to the unit circle. From this bifurcation, a new branch of solution emerges, featuring periodic solutions but with a doubled period with respect to the solution of the initial branch.

Neimark-Sacker bifurcations

This type of bifurcation takes place when the orbits have two complex conjugate characteristic multipliers, and the motion of the characteristic multipliers causes them to leave the unit circle, or contrarily to be limited on the unit circle. This class of bifurcations induces the generation of a new branch of quasi-periodic solutions. Quasi-periodic solutions are described by two different frequencies, a main one ω_1 and a secondary one ω_2 , which ratio is irrational. In the vicinity of the bifurcation, the pulsation ω_2 can be approximated by the imaginary part in the absolute value of the pair of Floquet exponents.

Real saddle bifurcations

This kind of bifurcation appears when the orbits have characteristic multipliers that cross the real axis, and the motion of the characteristic multipliers causes them to leave the real axis, or contrarily to be limited on the real axis.

A graphical representation of the behaviors of the Floquet multipliers for the discussed bifurcations is shown in **FIG. 2.9**.

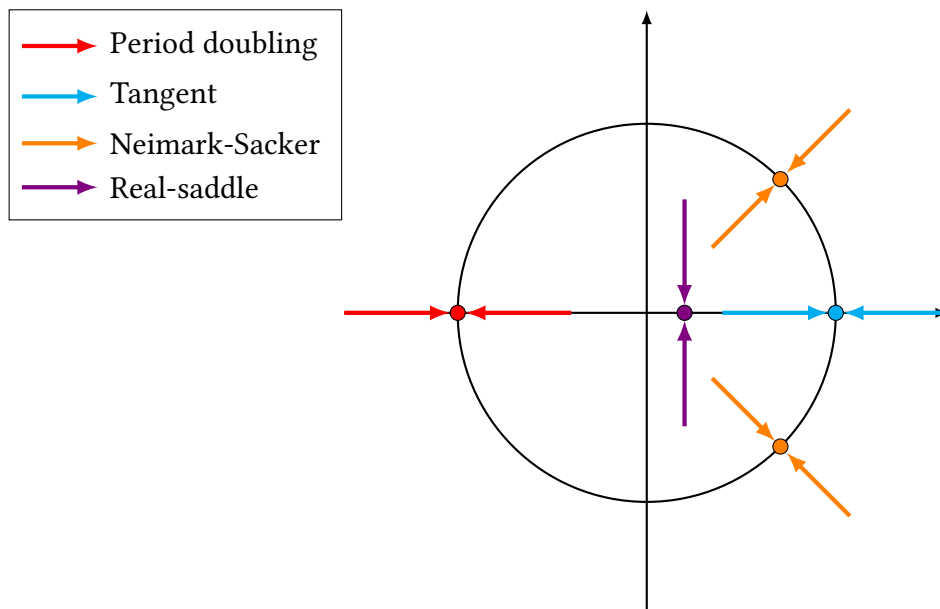


FIG. 2.9: Floquet multipliers evolution on the complex plane during the various bifurcations.

ManLab was used within the framework of this thesis for its efficient alternative application of the **HBM** and for its efficient continuation scheme. This chapter briefly provides the general ideas behind the algorithms used by the software. Furthermore, it contains a short analysis of two elementary examples in order to comprehend and showcase at best the recast and the initialization procedures.

3.1 Introduction

Since its first release, the package was used several times for various applications belonging to different engineering fields. One of its first applications aimed to analyze the radial responses of free encapsulated microbubbles excited by an ultrasonic plane wave [49]. The package was mostly used for the analysis of structural systems, and in some cases as verification method for original models. In particular, within this field it was exploited in order to study the dynamics of highly flexible slender structures [50] modeled via finite elements, to investigate the dynamics of bolted flange joints [51] in presence of large amplitude vibrations which induces complex non-linear behaviours due to the discontinuous nature of the joint and finally to investigate non-linear energy exchange in chains of non-linear oscillators [52] in which it was studied how branch points makes possible to transfer energy between non linear modes and how Neimark-Sacker bifurcations can lead to chaotic behaviours.

Furthermore, ManLab had been used for the automotive industry, in which it was firstly exploited with the aim of investigating quasi-static simulations of an assembly of flexible cables [53] modeled through a geometrically exact beam model. In particular, it was used for assessing the stability [54] as well as to propose new design guidelines [55] for centrifugal pendulum vibration absorbers.

3.2 Theory

ManLab [56] is a MATLAB [57] package, freely available for scientific use, for interactive continuation and bifurcation analysis of non linear system of equations of the form

$$\mathbf{R}(\mathbf{U}) = 0. \quad (3.1)$$

\mathbf{R} is a vector of n smooth equations and \mathbf{U} a vector of $n + 1$ unknowns.

The software provides algorithms for continuation, stability and bifurcation analysis of periodic orbits of a given dynamical system, using the harmonic balance method (HBM).

The continuation is based on the Asymptotic Numerical Method (ANM) [58]. At each continuation step, the branch solutions are given by a power series expansion with respect to the pseudo-arc length parameter. The main advantage of this method is that these series contain many useful information, making the continuation and the detection of bifurcation is extremely robust [59] and significantly easier than with classical predictor-corrector algorithms. The stability computation is based on the computation of the Floquet exponents in the frequency domain with a Hill eigenvalue problem.

3.2.1 Quadratic formulation of the Harmonic Balance Method

ManLab considers an autonomous system in the form

$$\dot{\mathbf{Y}} = \mathbf{f}(\mathbf{Y}, \lambda) \quad (3.2)$$

in which λ is a real parameter. It is assumed that the system has branches of periodic solutions when it varies.

Additionally, in order to provide a very simple and systematic algebra for the **HBM** application, it is based on the idea of recasting the original equations into a new system where the non-linearities are at most quadratic polynomials. This procedure was proven in [60] to be possible for a large class of systems with smooth equations, and extended to the case of non-polynomial nonlinearities in [61]. Therefore, the system will be written as follow:

$$m(\dot{Z}) = c + l(Z) + q(Z, Z). \quad (3.3)$$

Z (of size N_e) is the vector of unknowns containing the original components of the vector Y and some new variables which are added to obtain a quadratic form, c is a constant vector with respect to Z , $l(\cdot)$ and $m(\cdot)$ are a linear operator and $q(\cdot, \cdot)$ is a quadratic operator.

By introducing the expansion of Z computed as shown in **Eq. 2.38** into the set of **Eq. 3.3**, collecting the terms of the same harmonic index, and neglecting the higher order harmonics, one obtains a large system of $(2N_H + 1) \times N_e$ equations for the unknown vector U :

$$\omega \mathbf{M}(\mathbf{U}) = \mathbf{C} + \mathbf{L}(\mathbf{U}) + \mathbf{Q}(\mathbf{U}, \mathbf{U}). \quad (3.4)$$

The new operators $\mathbf{M}(\cdot)$, $\mathbf{C}(\cdot)$ and $\mathbf{Q}(\cdot, \cdot)$ depends only on the operators $m(\cdot)$, c , $l(\cdot)$ and $q(\cdot, \cdot)$ and on the number of harmonics N_H and are reported in [60].

This final system contains $(2N_H + 1) \times N_e$ equations for the $(2N_H + 1) \times N_e$ unknowns U plus the angular frequency ω and the continuation parameter λ .

3.2.2 Asymptotic Numerical Method

The Asymptotic Numerical Method (**ANM**) relies on a high-order Taylor series representation of the solution branch. Its efficiency was already demonstrated for many engineering application [62], mechanics [63] and acoustic. In ManLab, a quadratic workframe is available, as it was shown in the previous section. Therefore, the implementation is based on a quadratic formulation of the method. It is explained in detail in [64] and briefly reported in the following.

Taking into account the algebraic system

$$R(u, \lambda) = 0, \quad (3.5)$$

the technique to compute a continuation step is implemented as follows:

defining $\mathbf{U}_0 = (\mathbf{u}_0, \lambda_0)$ to be a regular solution of **Eq. 3.5**, it follows that the rank of the Jacobian matrix in the point U_0

$$\frac{\partial R}{\partial U} = \left[\frac{\partial R}{\partial u}, \frac{\partial R}{\partial \lambda} \right] \quad (3.6)$$

is N_{eq} . U_0 is taken as starting point of the continuation step. Defining $U_1 = (u_1, \lambda_1)$ as an unitary tangent vector at point U_0 and $a = (u - u_0) \cdot u_1 + (\lambda - \lambda_0) \cdot \lambda_1 = (U - U_0) \cdot U_1$ as the pseudo-arc length parameter, which is used as a closing equation for the system in **Eq. 3.5**. The analytic implicit function theorem allows to search the solution branch of the system around U_0 as a Taylor series expansion with respect to a

$$\mathbf{U}(a) = U_0 + aU_1 + a^2U_2 + a^3U_3 + \dots, \quad (3.7)$$

ensuring that λ is developed as a series of the path parameter a as well. The series are truncated at an arbitrary order p , which in general is set to 20. Consequently, \mathbf{U} is replaced in **Eq. 3.5** by its series expansion, giving the development of $R(U(a))$

$$R(U(a)) = R(U(0)) + aR_1 + a^2R_2 + a^3R_3 + \dots \quad (3.8)$$

in which

$$\begin{aligned} R_1 &= \left. \frac{dR}{da} \right|_{a=0} = \frac{\partial R}{\partial U} U_1 \\ R_2 &= \left. \frac{1}{2} \frac{d^2R}{da^2} \right|_{a=0} = \frac{\partial R}{\partial U} U_2 - F_2(U_1) \\ R_3 &= \left. \frac{1}{3!} \frac{d^3R}{da^3} \right|_{a=0} = \frac{\partial R}{\partial U} U_3 - F_3(U_1, U_2) \\ &\quad \vdots \quad \vdots \quad \vdots \\ R_p &= \left. \frac{1}{p!} \frac{d^pR}{da^p} \right|_{a=0} = \frac{\partial R}{\partial U} U_p - F_p(U_1, \dots, U_{p-1}). \end{aligned} \quad (3.9)$$

F_k are functions that only depend on the already computed terms of the series, leading the system in **Eq. 3.5** to be written as: $R_k = 0$, $\forall k \leq p$.

The domain of utility $[0, a_{max}]$ is determined when the series in **Eq. 3.7** is computed up to order p . The maximum increase of the residue in **Eq. 3.5** is set to a small value ϵ_1 , such that $\|R(U(a)) - R(U(0))\| < \epsilon_1$ for all $a \in [0, a_{max}]$. Using the approximation $R(U(a)) - R(U(0)) = a^{p+1}R_{p+1}$ yields

$$a_{max} = \left(\frac{\epsilon_1}{\|R_{p+1}\|} \right)^{\frac{1}{p+1}}. \quad (3.10)$$

The ending point of the continuation step $U(a_{max})$ is computed and used as the starting point of the next continuation step, leading to a continuous representation of the solution branch.

The **ANM** has the following advantages:

- The branch of solution is known analytically, section by section.
- Since all the linear systems to be solved have the same Jacobian matrix, the computational cost of the series in **Eq. 3.7** is low.
- The range of validity is computed automatically and without tuning parameter through **Eq. 3.10**. Both ϵ_1 and p do not alter the convergence, but only the accuracy, unlike to what happens in predictor-corrector method.
- The **ANM** benefits from the same robustness as the arc-length method even for sharp turns, due to the use of a pseudo arc-length measure as path parameter. Furthermore, for smooth

nonlinearities, it is rare to see a residue greater than $10\epsilon_1$ [65]. Even in the case of non-polynomial nonlinearities, a Newton-Raphson type correction step can be easily coupled with the method.

- The ANM has the ability to follow a branch even when a bifurcation occurs, allowing to achieve a complete description of the bifurcation diagram. A solution to switch from a branch to another is to perturb the initial problem as explained in [60].

3.2.3 Quadratic formulation of the Floquet-Hill stability

The Floquet-Hill method is implemented in ManLab, formulated for a quadratic workframe, as stated in [66] and summarised in the following.

Floquet theory states that the linear stability of a periodic solution $\mathbf{x}_0(t)$ can be studied by superimposing a small disturbance y such that $\mathbf{x}(t) = \mathbf{x}_0(t) + \mathbf{y}(t)$, satisfying the linearized system

$$\dot{\mathbf{y}} = \mathbf{J}(t)\mathbf{y}(t) \quad (3.11)$$

where \mathbf{J} is the Jacobian matrix of the system computed at a specific point.

The Hill's method is a frequency domain approach of the Floquet theory to solve Eq. 3.11. The analyzed system is recast in the quadratic form, with N_a auxiliary variables, and written in the frequency domain by expanding it on real Fourier basis of order N_H as seen in Section 3.2.1

$$\begin{cases} \omega\mathbf{M} = \mathbf{G}(\mathbf{X}, \mathbf{X}_a) \\ 0 = \mathbf{G}_a(\mathbf{X}, \mathbf{X}_a) \end{cases} \quad (3.12)$$

with

$$\begin{cases} \mathbf{G}(\mathbf{X}, \mathbf{X}_a) = \mathbf{C} + \mathbf{L}(\mathbf{X}_f) + \mathbf{Q}(\mathbf{X}_f, \mathbf{X}_f) \\ \mathbf{G}_a(\mathbf{X}, \mathbf{X}_a) = \mathbf{C}_a + \mathbf{L}_a(\mathbf{X}_f) + \mathbf{Q}_a(\mathbf{X}_f, \mathbf{X}_f) \end{cases} \quad (3.13)$$

In combination with the Floquet's form reported in [66], Eq. 3.13 yields

$$\begin{cases} \omega\mathbf{M}(\mathbf{P}) + \tilde{\lambda} = \mathbf{L}(\mathbf{P}_f) + \mathbf{Q}(\mathbf{X}_{f0}, \mathbf{P}_f) + \mathbf{Q}(\mathbf{P}_f, \mathbf{X}_{f0}) \\ 0 = \mathbf{L}_a(\mathbf{P}_f) + \mathbf{Q}_a(\mathbf{X}_{f0}, \mathbf{P}_f) + \mathbf{Q}_a(\mathbf{P}_f, \mathbf{X}_{f0}) \end{cases} \quad (3.14)$$

which, as being linear in \mathbf{P} and \mathbf{P}_a , can be written as

$$\begin{cases} \omega\mathbf{M}(\mathbf{P}) + \tilde{\lambda}\mathbf{P} = \frac{\partial\mathbf{G}}{\partial\mathbf{X}}\mathbf{P} + \frac{\partial\mathbf{G}}{\partial\mathbf{X}_a}\mathbf{P}_a \\ 0 = \frac{\partial\mathbf{G}_a}{\partial\mathbf{X}}\mathbf{P} + \frac{\partial\mathbf{G}_a}{\partial\mathbf{X}_a}\mathbf{P}_a \end{cases} \quad (3.15)$$

The second line of Eq. 3.15 allows to write \mathbf{P}_a as a function of \mathbf{P} . Replacing this expression in the first line of the equation, one obtains the following eigenvalue problem

$$(\mathbf{H} - \tilde{\lambda}\mathbf{I}_{N(2N_H+1)})\mathbf{P} = \mathbf{0} \quad (3.16)$$

which is the system in Eq. 3.11 projected on the Floquet forms in the frequency domain, and where \mathbf{H} is the Hill matrix:

$$\mathbf{H} = \frac{\partial\mathbf{G}}{\partial\mathbf{X}} - \frac{\partial\mathbf{G}}{\partial\mathbf{X}_a} \left[\frac{\partial\mathbf{G}_a}{\partial\mathbf{X}_a} \right]^{-1} \frac{\partial\mathbf{G}_a}{\partial\mathbf{X}} - \omega\mathbf{M}. \quad (3.17)$$

The Floquet multipliers are then obtained computing the eigenvalues of the Hill matrix.

3.3 Application on elementary examples

In order to understand how to set the equations of motion of a problem within the software, two simple examples are given. These examples will be used to demonstrate how to correctly set both a forced and, most importantly, an autonomous system. The quadratic recast procedure will be briefly clarified as well, as it represents the most difficult step of the analysis in many applications.

3.3.1 Initial conditions

Before starting with the examples and showing the recasting procedure, it is useful to clarify how to properly set the initial conditions, as this can be cumbersome in the most complex problem where the recast needs a high number of auxiliary variables.

The software requires three inputs from the user:

- The equation of the system, to be written in quadratic form in the @equations.m file.
- The starting value for λ and ω .
- The starting value for Z_0 .

The following expression is used:

$$\mathbf{Z}_0 = [\mathbf{v}_1 \ \mathbf{v}_2 \ \dots \ \mathbf{v}_n], \quad (3.18)$$

in which $\mathbf{v}_1 \ \dots \ \mathbf{v}_n$ are vectors containing the coefficients coming from the real Fourier decomposition for every variable $v_1 \ \dots \ v_n$ of the system under study. They are computed as

$$\begin{aligned} v_1(t) &= c_0 + \sum_{k=1}^{N_H} c_k \cos k\omega t + s_k \sin k\omega t \\ &\vdots \\ v_n(t) &= c_0 + \sum_{k=1}^{N_H} c_k \cos k\omega t + s_k \sin k\omega t \end{aligned} \quad (3.19)$$

and, therefore,

$$\begin{aligned} \mathbf{v}_1 &= [c_0 \ c_1 \ \dots \ c_{N_H} \ s_1 \ \dots \ s_{N_H}]^T \\ &\vdots \\ \mathbf{v}_n &= [c_0 \ c_1 \ \dots \ c_{N_H} \ s_1 \ \dots \ s_{N_H}]^T \end{aligned} \quad (3.20)$$

In simpler cases, such as the examples showed in this section, this \mathbf{Z}_0 matrix contains random values close to zero, with a magnitude that can be proportional to $10^{-7} \div 10^{-10}$. In these cases, Newton-Raphson initial iterations can be used to correct this guess in order to find a first periodic orbit from which the continuation starts.

However, in more complex cases, as the ones considered in this thesis, it is necessary that \mathbf{Z}_0 contains the coefficients of an already known periodic orbit, otherwise the Newton-Raphson initial iterations will never converge to a physical periodic orbit.

3.3.2 Forced Van der Pol oscillator

The forced Van der Pol oscillator is a simple problem, useful to grasp the concept of the quadratic recast. It is governed by the following equation of motion

$$\ddot{x} - \mu_1 \dot{x} + \mu_2 x \dot{x} + \mu_3 x^2 \dot{x} + a_1 x = f \cos \lambda t \quad (3.21)$$

which, in the case where $\mu_1 = \mu_2 = 0.1$, $f = \mu_3 = a_1 = 1$ shows periodic solutions. Defining a supplementary variable and an auxiliary one

$$\begin{aligned} y(t) &= \dot{x} \\ z &= x^2 \end{aligned} \quad (3.22)$$

it is possible to recast **EQ.** 3.21 in the following quadratic differential-algebraic system

$$\begin{cases} \dot{x} = y \\ \dot{y} = f \cos \lambda t + \mu_1 y - a_1 x - \mu_2 x y - \mu_3 y z \\ 0 = z - x^2 \end{cases} \quad (3.23)$$

In order to be correctly interpreted, **EQ.** 3.23 must be written as following within the `@equations.m` file, making sure to correctly insert in the correspondent vector the main part, the auxiliary part and the applied external force:

$$\begin{cases} 0 = y - \dot{x} \\ 0 = f \cos \lambda t + \mu_1 y - a_1 x - \mu_2 x y - \mu_3 y z - \dot{y} \\ 0 = z - x^2 \end{cases} \quad (3.24)$$

By adding a further equation in the `@launch.m` file, stating that $\lambda = \omega$, it is possible to set the pulsation of the external force as the continuation parameter. The starting point of the continuation is set by stating the initial value of λ , which in this case is set to zero.

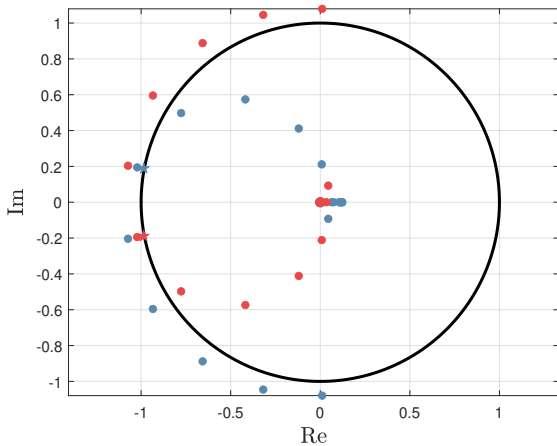


FIG. 3.1: Evolution on the complex plane of the Floquet multipliers during the continuation of the solution branch.

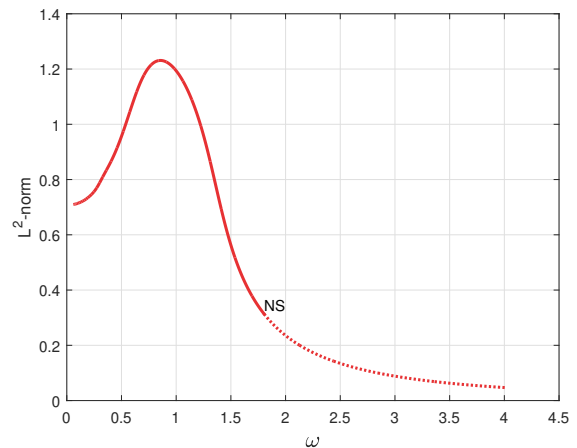


FIG. 3.2: L2 Norm of the x variable.

FIG. 3.1 displays the evolution of the floquet multipliers on the complex plane during the continuation of the solution. The star icon shows the position of the detected Neimark-Sacker bifurcation.

The position of the bifurcation is also exhibit in **FIG. 3.2**, it is shown as the solution passes from stable (continuous line) to unstable (dashed line). The bifurcation takes place when $\lambda = 1.804$. It is finally possible to visualise the orbits produced in the phase space as illustrated in **FIG. 3.3**.

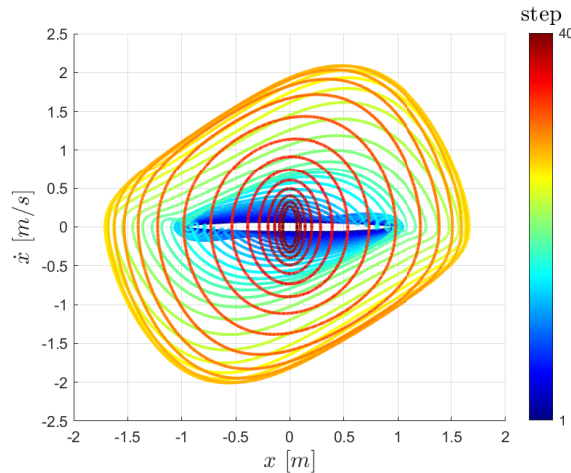


FIG. 3.3: Van der pol phase space evolution during the continuation.

The color map in the figure shows at which step of the continuation the orbit belongs to, colors towards blue belong to earlier steps while red colors belong to latest steps. It can clearly be seen that the shape of the family suddenly changes after the Neimark-Sacker bifurcation.

3.3.3 Free nonlinear pendulum

As the problems of interest of this thesis are autonomous, it is important to understand how to properly set them in the software.

Defining θ as the angle between the present position of the pendulum and its lower rest position, the equation of motion of the free pendulum, neglecting the coefficients, is

$$\ddot{\theta} + \sin \theta = 0. \quad (3.25)$$

In general periodic orbits of conservative Hamiltonian systems belong to an one dimensional family of periodic solutions, having as parameter the value of the first integral. This parameter is not explicit in the system, as shown in [67]. Therefore, in order to compute the family of periodic solutions, in the standard continuation framework presented in this chapter, it is necessary to perturb the equation by adding a damping term, also called unfolding term,

$$\ddot{\theta} + \lambda \dot{\theta} + \sin \theta = 0, \quad (3.26)$$

where λ is a free parameter of the continuation. The periodic orbits of the perturbed system are exactly the same as the ones of the unperturbed system if and only if $\lambda = 0$. Doing so, the parameter λ allows to compute the periodic orbits of the conservative system by using the classical framework for dissipative systems which possess an explicit control parameter.

Using the three supplementary variables

$$\begin{aligned} y(t) &= \dot{\theta} \\ s(t) &= \sin \theta \\ c(t) &= \cos \theta \end{aligned} \quad (3.27)$$

the last two lines being auxiliary, it is possible to recast **EQ. 3.26** into the following quadratic, differential-algebraic system:

$$\begin{cases} 0 = y - \dot{\theta} \\ 0 = -s - \lambda y - \dot{y} \\ 0 = cy - \dot{s} \\ 0 = -sy - \dot{c} \end{cases} \quad (3.28)$$

As the non-linearity is non-algebraic, in addition this system needs the following initial conditions, to fall back to the case of a quadratic recast as explained in [61]

$$\begin{cases} s(0) = \sin \theta(0) \\ c(0) = \cos \theta(0) \end{cases} \quad (3.29)$$

Using **EQ. 3.28** in the software, following the same treatment of the previous case, with the corresponding initial conditions, and starting from a first point having $\lambda = 10^{-9}$ and $\omega = 1$, it is possible to obtain the results presented in **FIG. 3.4** and in **FIG. 3.5**.

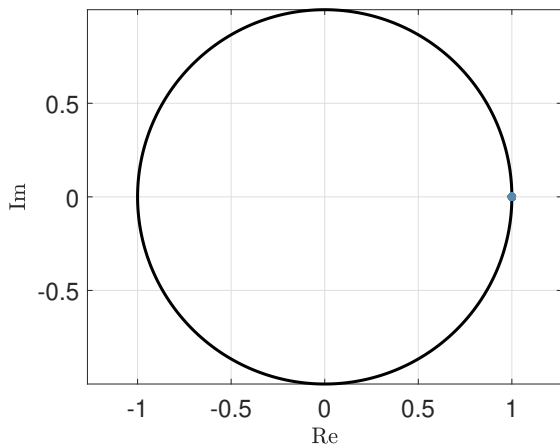


FIG. 3.4: Evolution on the complex plane of the Floquet multipliers during the continuation of the solution branch.

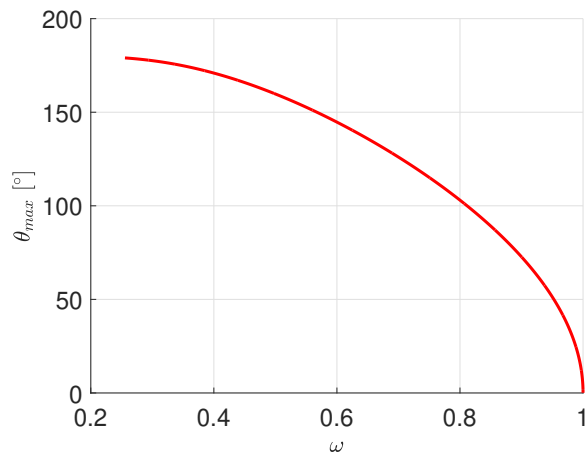


FIG. 3.5: θ_{max} for each pulsation value.

The Floquet multipliers are fixed in the complex plane. Therefore, as expected the system always remains stable during the continuation. **FIG. 3.5** shows that the maximum angle of the pendulum decrease while the pulsation increase, which physically means that for larger amplitudes of the oscillation the period increases, as expected from practical experience.

In order to better visualise the results also the phase space is displayed in **FIG. 3.6**,

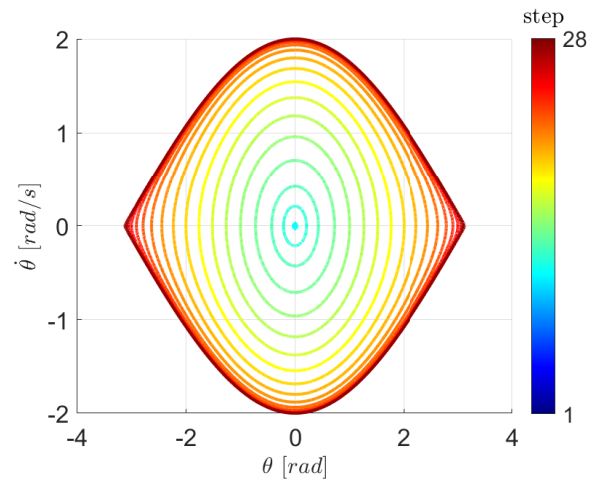


FIG. 3.6: Free pendulum phase space evolution during the continuation.

showing the orbits correspondent to each step of the continuation. It can be seen how the orbits start from a small oscillation around the rest position and while the pulsation decrease they asymptotically tend to the orbit in which the maximum angle is reached.

Validation

This chapter concern the validation of the selected method for the computation of the gravitational potential presented in Section 2.2.2, as well as the validation of ManLab.

4.1 Gravitational potential model

The validation of the gravitational potential computation is of drastic importance, as it is the fundamental building block of the study. Therefore, in order to attest its validity it will be tested both comparing it to the Earth gravitational potential and most importantly by comparing the results around irregular-shaped bodies.

4.1.1 Earth gravity

The first part of the validation of the Earth gravitational field is carried by comparing its gravitational acceleration computed both analytically with **Eq. 4.1** and through the polyhedron method using **Eq. 4.2**:

$$g = \frac{GM_{\oplus}}{r^2}. \quad (4.1)$$

G is the universal gravitational constant, M_{\oplus} is the Earth's mass and r is the distance from its center, and

$$g = |\nabla U|, \quad (4.2)$$

where ∇U is computed using **Eq. 2.28**.

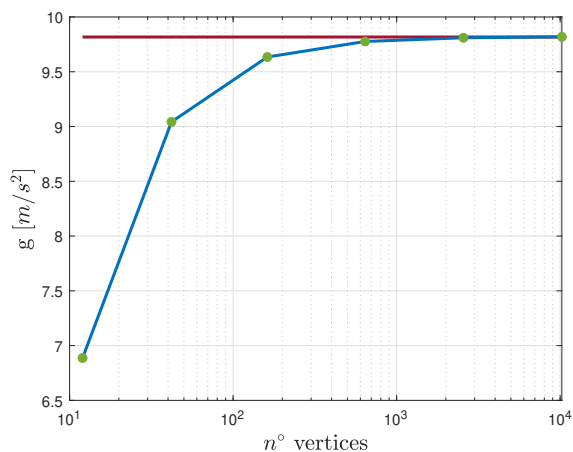


FIG. 4.1: Analytical and polyhedral sea level gravitational acceleration changing the number of the vertices of the polyhedron.

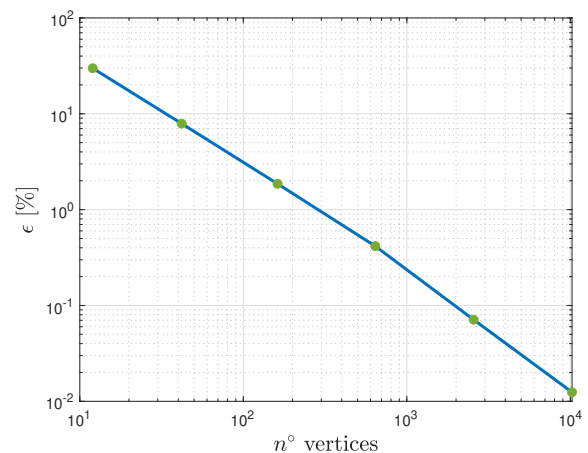


FIG. 4.2: Percentual relative error between the two methods.

FIG. 4.1 shows in red the analytical value of the gravitational acceleration at sea level, while its values computed using a polyhedron with respectively 12, 42, 162, 642, 2562 and 10242 vertices are displayed in blue and green.

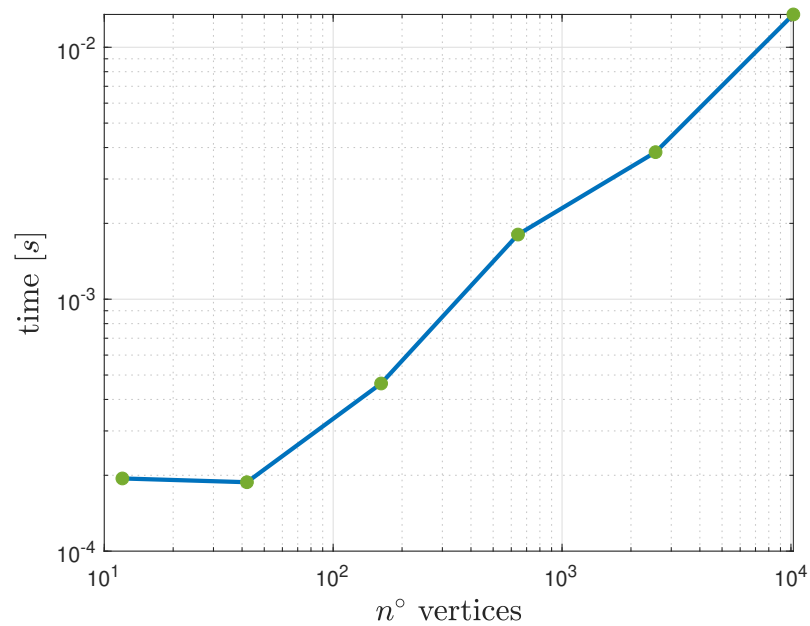


FIG. 4.3: Computation time to perform the calculation to polyhedron with different number of vertices.

FIG. 4.3 shows the computational time taken by for each polyhedron model to compute the gradient of the gravitational potential in one point, displaying how the order of magnitude quickly rises with the number of vertices. Therefore, a trade-off between the committed percentual error and the computational time leads to the choice of the polyhedral model having 2562 vertices for the next step of the validation. This consist of computing the error between **EQ. 4.1** and **EQ. 4.2** for a polyhedron having 2562 vertices at different altitudes from the Earth's surface.

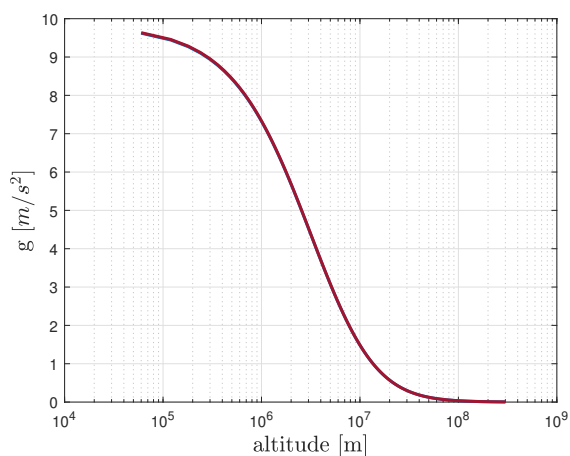


FIG. 4.4: Analytical and polyhedral gravitational acceleration comparison at different altitudes.

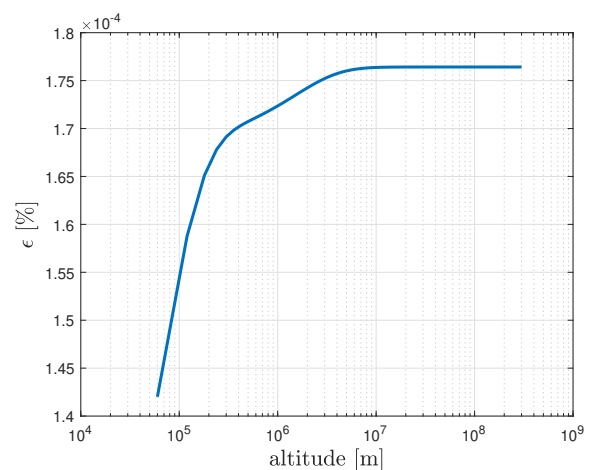


FIG. 4.5: Percentual relative error between the two methods.

FIG. 4.4 presents the gravitational attraction computed analytically in red and in blue by using the polyhedral model. As shown by **FIG. 4.5**, the error always stays below 10^{-4} %, reaching a plateau above an altitude of 8000 km.

The final validation test for the polyhedral model on the Earth is performed by comparing the time integration of the analytical classical two-body problem

$$\ddot{\mathbf{r}} = -\frac{\mu}{r^3}\mathbf{r}, \quad (4.3)$$

and the time integration of the two-body polyhedral model

$$\ddot{\mathbf{r}} = \nabla U(\mathbf{r}), \quad (4.4)$$

propagating the **ISS** orbit, having the initial Keplerian elements presented in **TAB. 4.1**.

TAB. 4.1 Two body problem validation orbit initial keplerain elements.

\mathbf{a} [m]	\mathbf{e} [-]	\mathbf{i} [°]	$\mathbf{\Omega}$ [°]	$\mathbf{\omega}$ [°]	$\mathbf{\theta}$ [°]
6699812	0.000357	51.6432	92.1296	315.04	0

The results for a propagation lasting 16 periods are presented in **FIG. 4.6** to **FIG. 4.11**.

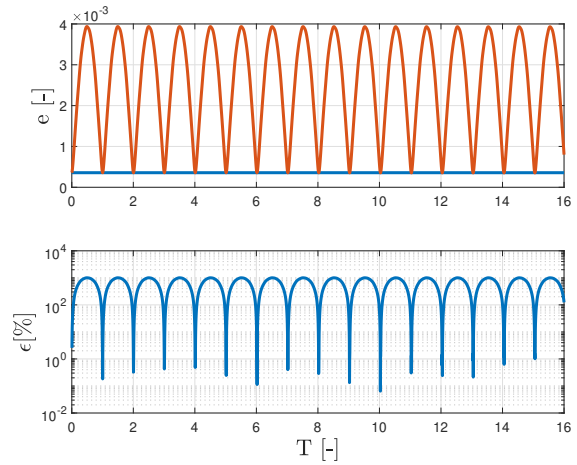
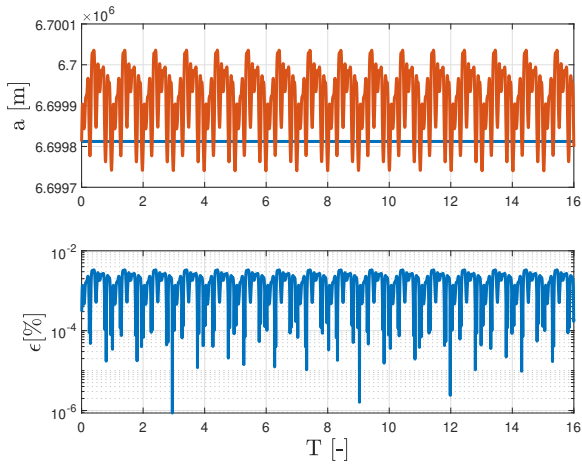


FIG. 4.6: Semi-major axis computed from the analytical and the polyhedral propagation and their relative error.

FIG. 4.7: Eccentricity computed from the analytical and the polyhedral propagation and their relative error.

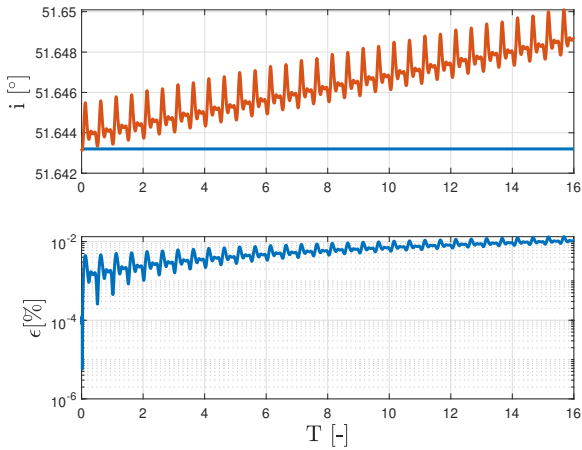


FIG. 4.8: Inclination computed from the analytical and the polyhedral propagation and their relative error.

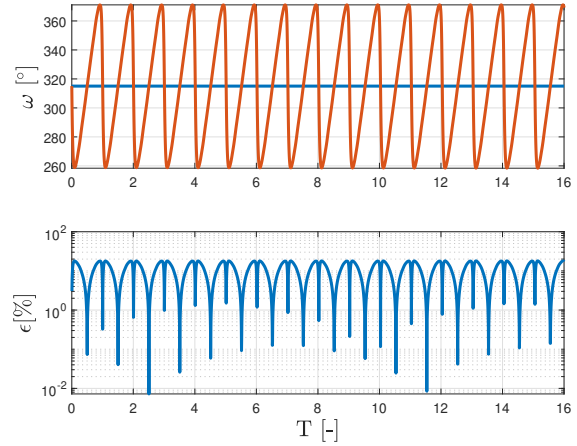


FIG. 4.9: Pericenter argument computed from the analytical and the polyhedral propagation and their relative error.

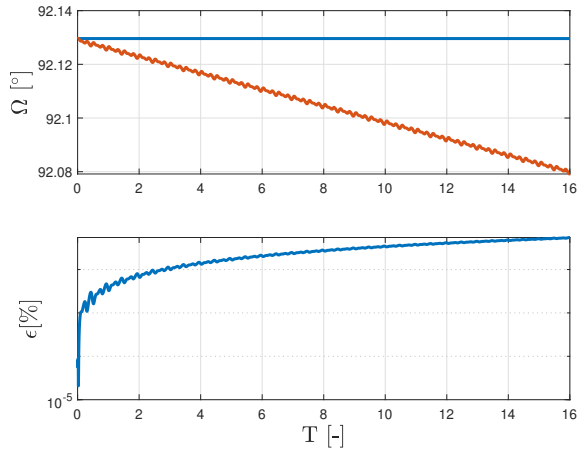


FIG. 4.10: Right ascensions of the ascending node computed from the analytical and the polyhedral propagation and their relative error.

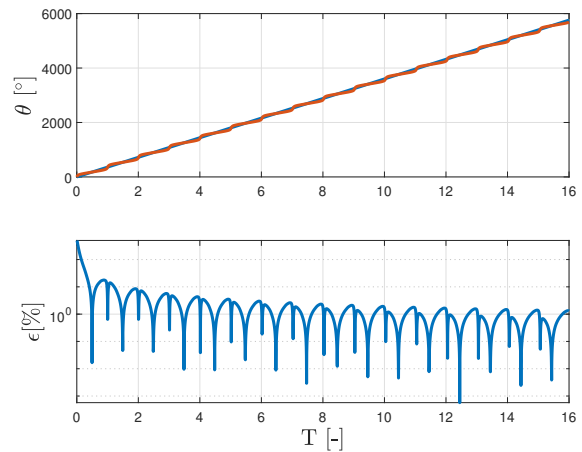


FIG. 4.11: True anomaly computed from the analytical and the polyhedral propagation and their relative error.

As shown, the error on all the Keplerian elements is contained, and the result of the method used to generate the mesh of the sphere, which was generated starting from an icosphere. The resulting periodic oscillations are similar to the oscillation that would result when the J_2 perturbation is accounted for.

4.1.2 Asteroid potential

With the propagation of an orbit around Earth, the gravitational potential was validated only for symmetrical bodies. However, it is also necessary to validate it for irregular-shaped bodies, as most of the known asteroids are not symmetrical and as symmetrical bodies could filter out errors that takes place in symmetrical point of the body.

As stated by **Eq. 2.20**, the position of the equilibrium points is the direct result of the gravitational potential around the body. It follows that two asteroids having the same equilibrium points and the same shape also have the same gravitational field. This property can be exploited for the validation, taking as reference the results presented in [68] for the asteroid *1996 Hw1*, being one of the most irregular-shaped body available in the study. In order to provide a larger pool for the control *4769 Castalia* and *6489 Golevka* are also taken into account.

TAB. 4.2 Reference and computed equilibrium points of *1996 Hw1* and their absolute error.

\mathbf{P}_e	$\mathbf{x}_{ref} [m]$	$\mathbf{x} [m]$	$\mathbf{y}_{ref} [m]$	$\mathbf{y} [m]$	$\mathbf{z}_{ref} [m]$	$\mathbf{z} [m]$	$\epsilon_x [m]$	$\epsilon_y [m]$	$\epsilon_z [m]$
1	3211.970	3211.993	133.831	134.251	-2.327	-2.642	0.023	0.420	0.315
2	-150.078	-150.186	2807.890	2807.946	0.515	0.249	0.108	0.056	0.265
3	-3268.660	-3268.624	84.143	84.467	-1.032	-1.347	0.035	0.324	0.314
4	-181.051	-181.056	-2826.050	-2825.985	0.146	0.058	0.005	0.064	0.087
5	452.595	452.643	-29.186	-29.075	3.020	2.934	0.048	0.111	0.085

TAB. 4.3 Reference and computed equilibrium points of *4769 Castalia* and their absolute error.

\mathbf{P}_e	$\mathbf{x}_{ref} [m]$	$\mathbf{x} [m]$	$\mathbf{y}_{ref} [m]$	$\mathbf{y} [m]$	$\mathbf{z}_{ref} [m]$	$\mathbf{z} [m]$	$\epsilon_x [m]$	$\epsilon_y [m]$	$\epsilon_z [m]$
1	910.109	910.031	22.864	22.645	34.592	34.448	0.077	0.219	0.143
2	-42.781	-42.610	736.033	735.912	3.128	3.010	0.170	0.120	0.118
3	-953.021	-952.843	128.707	128.996	30.065	30.036	0.178	0.289	0.028
4	-39.953	-40.215	-744.131	-743.967	8.762	8.599	0.261	0.163	0.162
5	157.955	158.146	-1.448	-1.449	-12.941	-13.087	0.191	0.001	0.145

TAB. 4.4 Reference and computed equilibrium points of *6489 Golevka* and their absolute error.

\mathbf{P}_e	$\mathbf{x}_{ref} [m]$	$\mathbf{x} [m]$	$\mathbf{y}_{ref} [m]$	$\mathbf{y} [m]$	$\mathbf{z}_{ref} [m]$	$\mathbf{z} [m]$	$\epsilon_x [m]$	$\epsilon_y [m]$	$\epsilon_z [m]$
1	-23.416	-22.528	-564.128	-564.150	-2.882	-3.002	0.887	0.022	0.120
2	35.808	36.218	571.527	571.515	-6.081	-6.214	0.410	0.011	0.133
3	537.470	537.508	21.647	21.546	-1.060	-1.269	0.038	0.100	0.209
4	-546.646	-546.632	26.365	26.039	-0.182	-0.364	0.013	0.325	0.182
5	-3.329	-3.284	-2.330	-2.311	2.198	2.075	0.044	0.018	0.122

As shown in **TAB. 4.2** to **TAB. 4.4**, the absolute error between the coordinates of the equilibrium points, computed by implementing the polyhedral gravitational model and the coordinates taken from the reference is well below 1 m for every asteroid taken into account. It is possible to conclude that the gravitational potential is valid and it can be used within ManLab.

4.2 ManLab

Once again the classical two body problem reported in **Eq. 4.3** is considered for the validation of the software, as it also represents a preliminary proof that it will be able to deal with more complex autonomous systems. First, the system must be written in quadratic form, and, for a better convergence, it is also necessary to re-scale the equations, yielding

$$\ddot{\tilde{\mathbf{r}}} = -\frac{T_0^2}{L_0^3} \frac{\mu}{\tilde{r}^3} \tilde{\mathbf{r}}, \quad (4.5)$$

where the characteristic unit of length and of time are $L_0 = R_e$ and $T_0 = \sqrt{\frac{L_0^3}{\mu}}$ respectively. Consequently, $\frac{T_0^2}{L_0^3}\mu = 1$, therefore, by using \mathbf{r} instead of $\tilde{\mathbf{r}}$ for an easier notation, and including the unfolding term as shown in Section 3.3.3, the following equation to be recast is obtained

$$\ddot{\mathbf{r}} = -\frac{\mathbf{r}}{r^3} - \lambda\dot{\mathbf{r}}. \quad (4.6)$$

By using four auxiliary variables

$$\begin{cases} v_1 = x^2 + y^2 + z^2 \\ v_2 = \sqrt{v_1} \\ v_3 = v_1 v_2 \\ v_4 = \frac{1}{v_3} \end{cases}, \quad (4.7)$$

the system of equations can be written as

$$\begin{cases} 0 = u - \dot{x} \\ 0 = v - \dot{y} \\ 0 = w - \dot{z} \\ 0 = -\lambda u - v_4 x - \dot{u} \\ 0 = -\lambda v - v_4 y - \dot{v} \\ 0 = -\lambda w - v_4 z - \dot{w} \\ 0 = v_1 - x^2 - y^2 - z^2 \\ 0 = v_1 - v_2^2 \\ 0 = v_3 - v_1 v_2 \\ 0 = 1 - v_4 v_3 \end{cases}. \quad (4.8)$$

Having recast the equations, is now possible to set the orbit that have the Keplerian parameters reported in **TAB. 4.5** and shown in **FIG. 4.12**, as initial condition of the continuation procedure applying the method explained in Section 3.3.1.

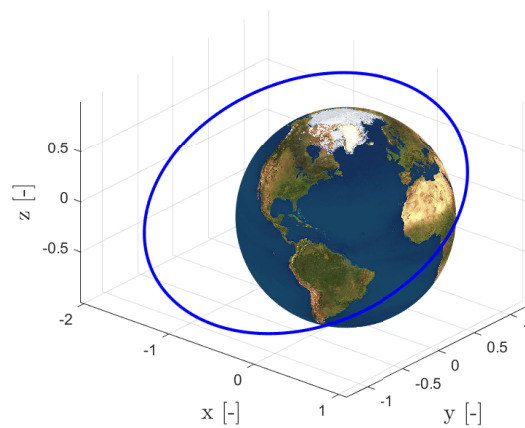
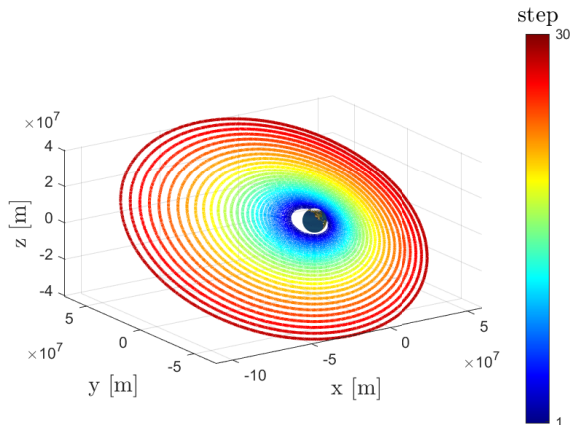
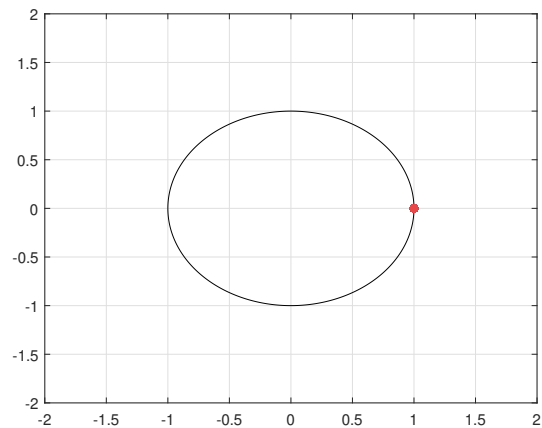


FIG. 4.12: Initial two body problem orbit for the ManLab validation.

TAB. 4.5 Initial two body problem orbit for the ManLab validation.

\mathbf{a} [m]	\mathbf{e} [-]	\mathbf{i} [°]	$\mathbf{\Omega}$ [°]	$\mathbf{\omega}$ [°]
10000000	0.3	30	0	0

By applying the continuation for 30 steps and using only the first 30 harmonics of the Fourier development, it is observed that Newton-Raphson iterations are not necessary to keep a residual proportional to 10^{-10} . This means that the recast is correct, and the results presented in **FIG. 4.13** and **FIG. 4.14** can be obtained.

**FIG. 4.13:** Two body problem ManLab continuation.**FIG. 4.14:** Evolution on the complex plane of the Floquet multipliers during the continuation of the solution branch.

As expected, the family of orbits remains always stable, also shown by the Floquet multipliers evolution reported in **FIG. 4.14**, which shows that the multipliers are located at +1 and stay fixed during the continuation. Moreover, the shape of the orbit remains the same. This is due to the fact that during the continuation, only the energy and, therefore the semi-major axis, is increasing.

For every orbit of the family, a point is selected and propagated in time for an entire period. After this propagation, the Keplerian elements computed from the ManLab results are compared to the ones computed from the last point of the time integration in order to assess the correctness of the software. The results are presented in **FIG. 4.15** to **FIG. 4.19**.

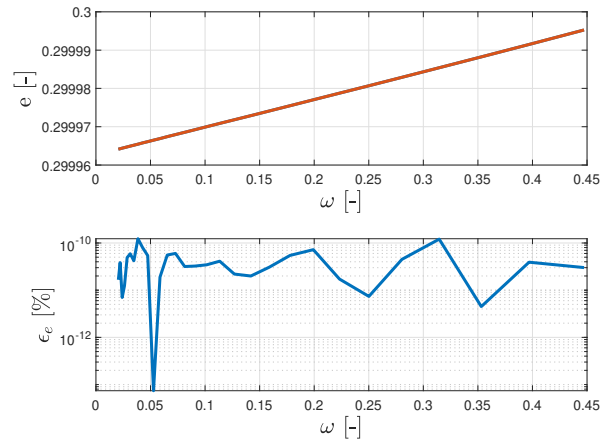
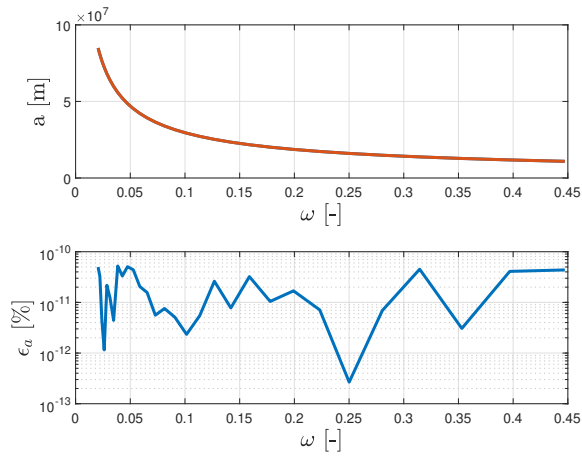


FIG. 4.15: Semi-major axis computed from ManLab and **FIG. 4.16:** Eccentricity computed from ManLab and time integration and their relative error.

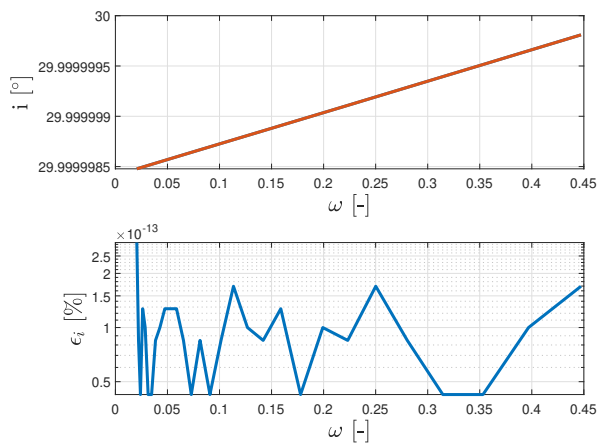


FIG. 4.17: Inclination computed from ManLab and time integration and their relative error.

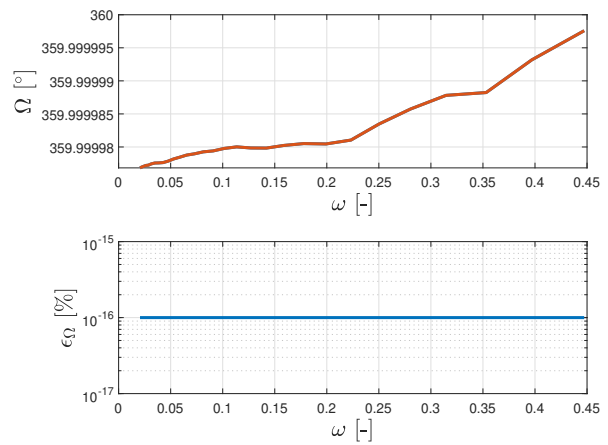


FIG. 4.18: Right ascension of the ascending node computed from ManLab and time integration and their relative error.

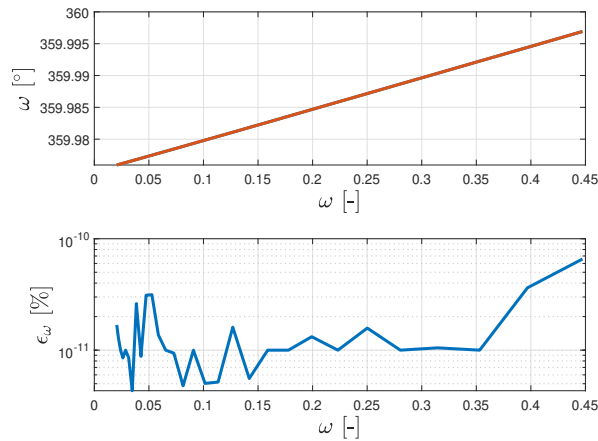


FIG. 4.19: Pericenter argument computed from ManLab and time integration and their relative error.

These figures show the trend of the Keplerian parameters along the continuation at every value of the orbit pulsation.

Once again, confirm that the semi-major axis is the only changing parameter, while the other parameters only see a negligible variation. Moreover, the percentual relative error between the parameters computed starting from ManLab and the one computed starting from time integration is at worst proportional to $10^{-10}\%$. Therefore, it is possible to prove that the orbits computed by ManLab coincide with the ones computed through time integration.

Application

In this chapter ManLab is finally applied to the **CR3BP** and to the asteroid problem. A detailed procedure for the recast of the equations is included for both problems, as it is complex for these two cases. Finally for the **CR3BP** the family of orbits around the L_1 equilibrium point are analyzed. While the asteroid problem analysis is more focused on the comparison to time integration and to the **HBM**.

5.1 Circular restricted three body problem

For this problem the most interesting families of orbits are the ones around the three collinear Lagrangian points. The analysis of this thesis focus mainly on the L_1 family and its bifurcations. However, before it is necessary to introduce in detail the quadratic recast procedure.

5.1.1 Recast

Starting from the system of equations given in **Eq. 2.2**, the procedure is similar to the one applied to the two body problem in Section 4.2. The only difference is that the problem was already re-scaled. Adding the unfolding term λ to the fourth, fifth and sixth equations in **Eq. 5.2**, and the following eight auxiliary variables

$$\left\{ \begin{array}{l} v_1 = (x + \mu)^2 + y^2 + z^2 \\ v_2 = [x - (1 - \mu)]^2 + y^2 + z^2 \\ v_3 = \sqrt{v_1} \\ v_4 = \sqrt{v_2} \\ v_5 = v_1 v_3 \\ v_6 = v_2 v_4 \\ v_7 = \frac{1}{v_5} \\ v_8 = \frac{1}{v_6} \end{array} \right. \quad (5.1)$$

, the set of equations describing the final recast system are

$$\left\{ \begin{array}{l} 0 = u - \dot{x} \\ 0 = v - \dot{y} \\ 0 = w - \dot{z} \\ 0 = -\lambda u + x + 2v - (1 - \mu)\mu v_7 + (\mu - \mu^2)v_8 - (1 - \mu)v_7x - \mu v_8x - \dot{u} \\ 0 = -\lambda v + y - 2u - (1 - \mu)v_7y - \mu v_8y - \dot{v} \\ 0 = -\lambda w - (1 - \mu)v_7z - \mu v_8z - \dot{w} \\ 0 = v_1 - (x + \mu)^2 - y^2 - z^2 \\ 0 = v_2 - [x - (1 - \mu)]^2 - y^2 - z^2 \\ 0 = v_1 - v_3^2 \\ 0 = v_2 - v_4^2 \\ 0 = v_5 - v_1v_3 \\ 0 = v_6 - v_2v_4 \\ 0 = 1 - v_5v_7 \\ 0 = 1 - v_6v_8 \end{array} \right. \quad (5.2)$$

In order to better analyse the results, the attention will be set on the families of orbits around the first Lagrangian point L_1 , while families around the L_2 and L_3 points are reported in the appendix.

5.1.2 Families around L_1 Lagrange point

Lyapunov

The continuation of the **L1** family, truncating the Fourier series to account for the contribution of only the first 30 harmonics, leads to the results depicted in **FIG. 5.1** reporting the shape of the orbits. **FIG. 5.2** represents the value of the Jacobi constant at each frequency of the continuation.

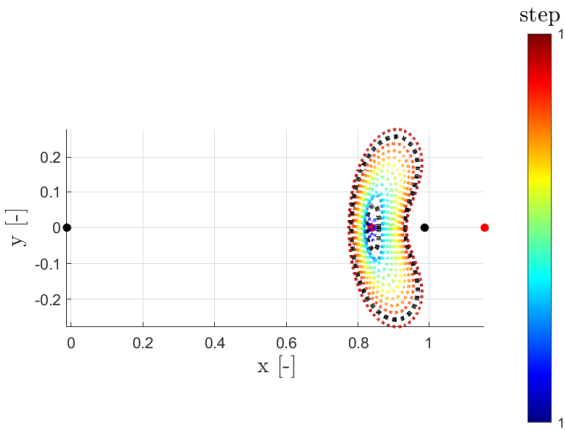


FIG. 5.1: L1 family computed through ManLab accounting 30 harmonics.

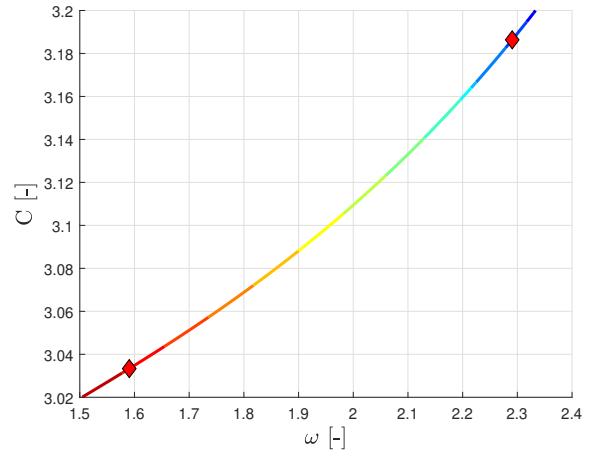


FIG. 5.2: Jacobi constant vs orbit frequency along the continuation.

As shown in **FIG. 5.2** and in **FIG. 5.3**, during the continuation, from high to low frequencies, two bifurcations were detected with the respective orbits reported in black in **FIG. 5.1**.

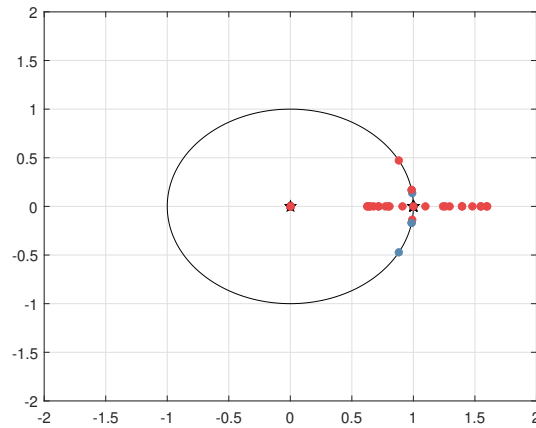


FIG. 5.3: Evolution on the complex plane of the Floquet multipliers during the continuation of the **L1** family.

The Floquet multipliers provide important information. The family is unstable, as one multiplier is not located within the unit circle. The first bifurcation at $\omega = 2.29$ is a tangent bifurcation, therefore, the multipliers join the unit circle through $+1$. Further in the continuation, the second bifurcation takes place at $\omega = 1.59$ and, in this case, the multipliers move along the unit circle, eventually merging at -1 and corresponding to a period-doubling bifurcation.

Unfortunately, it was not possible to detect this last bifurcation, as 30 harmonics were only enough to approximate the dynamics up to the second bifurcation. However, by increasing the number of harmonics, it is possible to compute the whole family at the cost of a much higher computation time.

Indeed, when accounting for 200 harmonics, it was possible to obtain the results shown in **FIG. 5.4** and in **FIG. 5.5**, depicting the whole family and its Jacobi constant, for which the computation of the stability was not computed as too heavy for the used computation system.

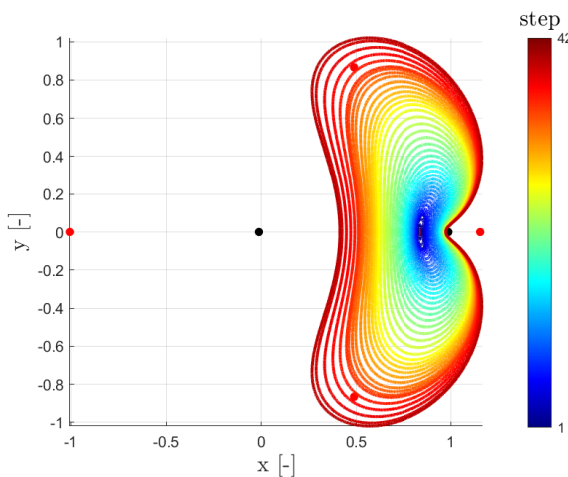


FIG. 5.4: **L1** family computed through ManLab accounting for 200 harmonics.

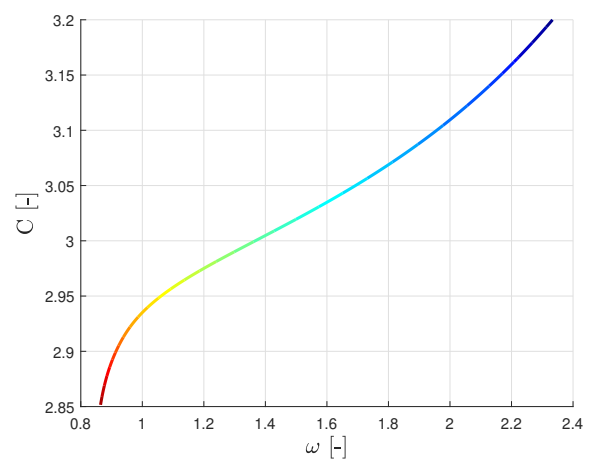


FIG. 5.5: Jacobi constant vs orbit frequency along the continuation.

Halo

The **H1** family is obtained following the branch emerging from the first **L1** bifurcation. Once again, the continuation is performed accounting only the first 30 harmonics to ease the stability computation, obtaining the results presented in **FIG. 5.6** and **FIG. 5.7**.

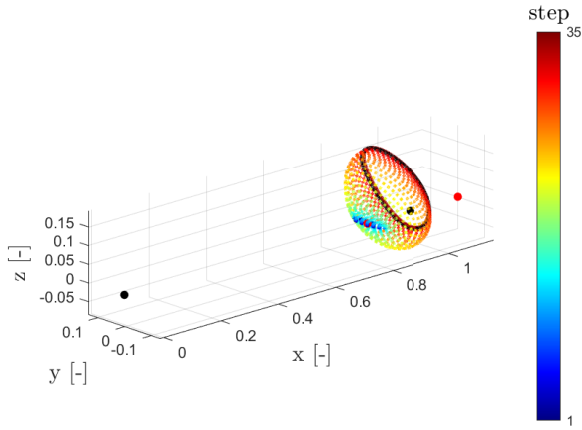


FIG. 5.6: **H1** family computed through ManLab accounting 30 harmonics.

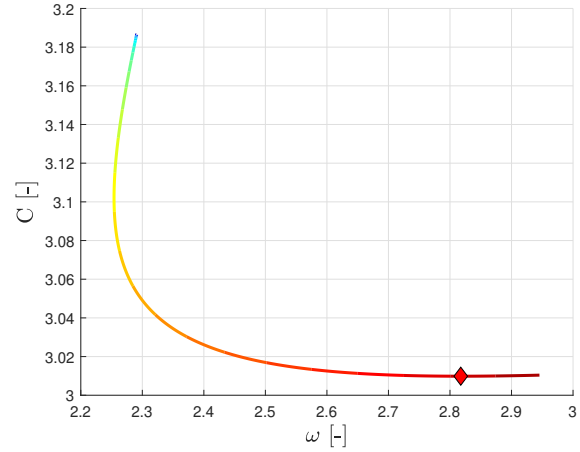


FIG. 5.7: Jacobi constant vs orbit frequency along the continuation.

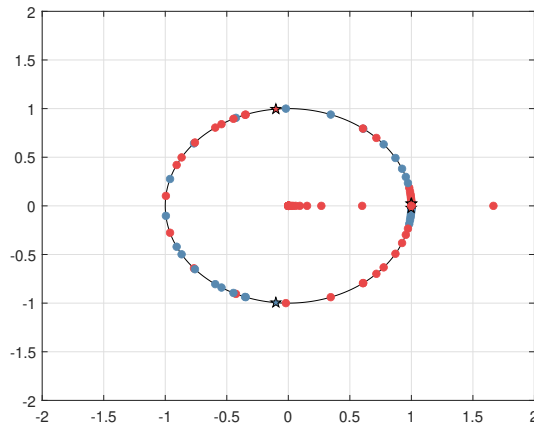


FIG. 5.8: Evolution on the complex plane of the Floquet multipliers during the continuation of the **H1** family.

The evolution of the multipliers in **FIG. 5.8** shows that the family is unstable at the starting point. With the multipliers travelling on the unit circle starting from +1 towards -1, the unstable multipliers re-joins the circle at +1 when the tangent bifurcation is detected at $\omega = 2.81$. After this bifurcation, due to the number of harmonics, the continuation follows a different family of orbits around the second mass. Once again, to compute the whole family, it was necessary to increase to 200 the number of harmonics. The result is presented in **FIG. 5.9**.

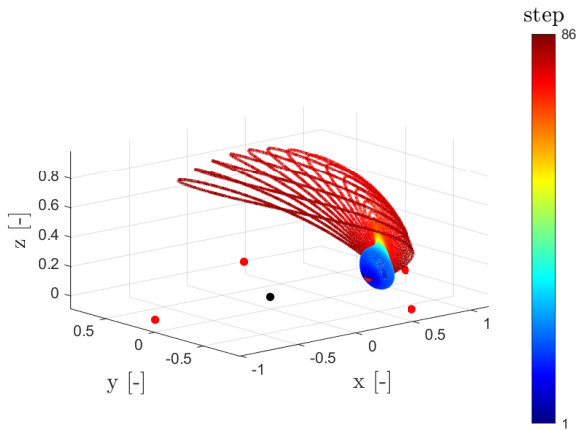


FIG. 5.9: H1 family computed through ManLab accounting for 200 harmonics.

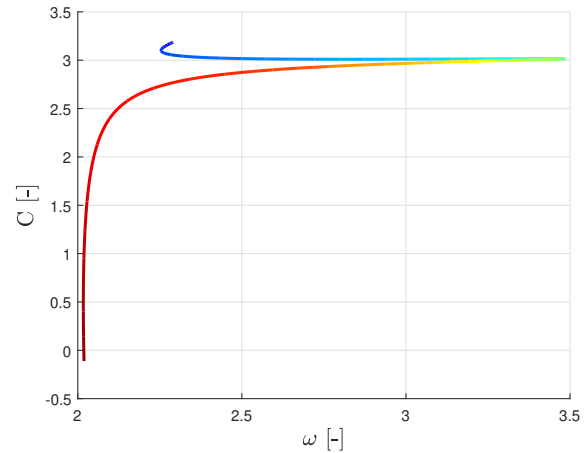


FIG. 5.10: Jacobi constant vs orbit frequency along the continuation.

Some interesting features can be deduced from **FIG. 5.10**. The frequency of the orbits is increased towards the resonant ratio 2:1, meaning that the period of these orbits is twice the period of the system. After this, the frequency decreases towards the 3:1 resonant ratio, with a strong decrease in the associated energy.

Axial

The **A1** family emerges from the second bifurcation of the **L1** family. Unlike to the previous two families, 30 harmonics were enough for a good representation of the dynamics of this family. An ulterior difference with the other families is that the **A1** family is quite short. It just consists of two branching points, the first where it emerges from the **L1** and the second where the **V1** emerges from it. The results of the continuation are presented in **FIG. 5.11** and in **FIG. 5.12**.

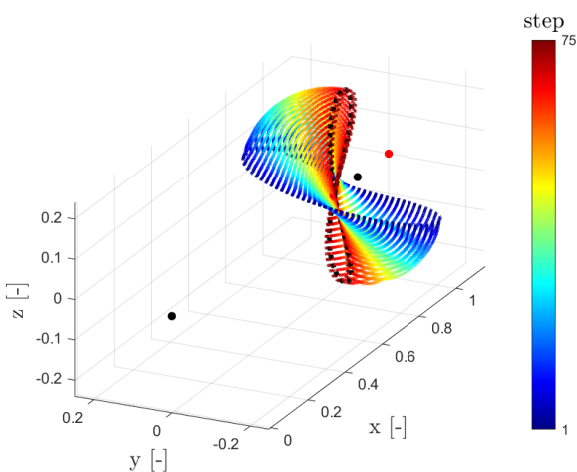


FIG. 5.11: A1 family computed through ManLab accounting 30 harmonics.

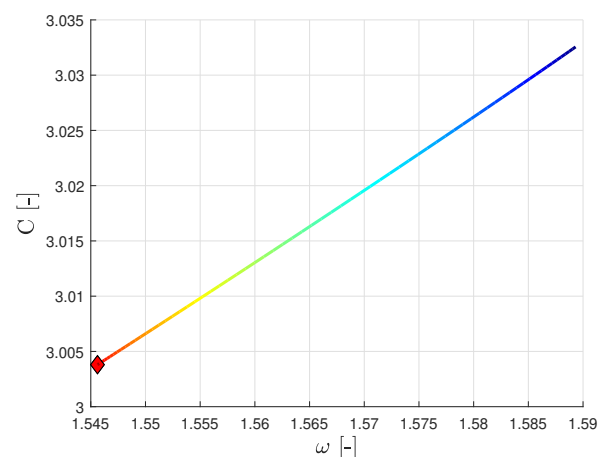


FIG. 5.12: Jacobi constant vs orbit frequency along the continuation.

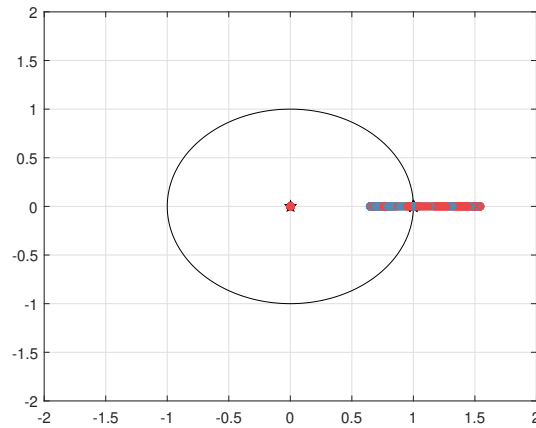


FIG. 5.13: Evolution on the complex plane of the Floquet multipliers during the continuation of the **A1** family.

All the orbits are unstable, as also shown in **FIG. 5.13**. It can be observed that the multipliers move towards and cross the $+1$ unit circle without stopping on it, with the tangent bifurcation taking place during this cross at $\omega = 1.54$.

Vertical

The **V1** family is the last one taking place around the L_1 Lagrange point and, as shown previously, it bifurcates from the **A1** family. Also in this case, taking only 30 harmonics into account was enough to compute the whole family and its the stability. The results are reported in **FIG. 5.14** and **FIG. 5.15**.

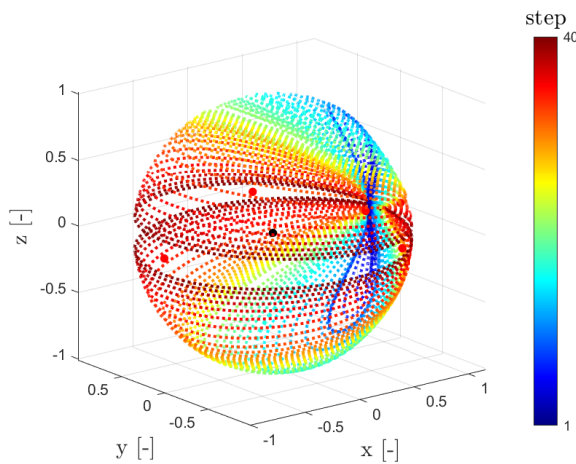


FIG. 5.14: **V1** family computed through ManLab accounting 30 harmonics.

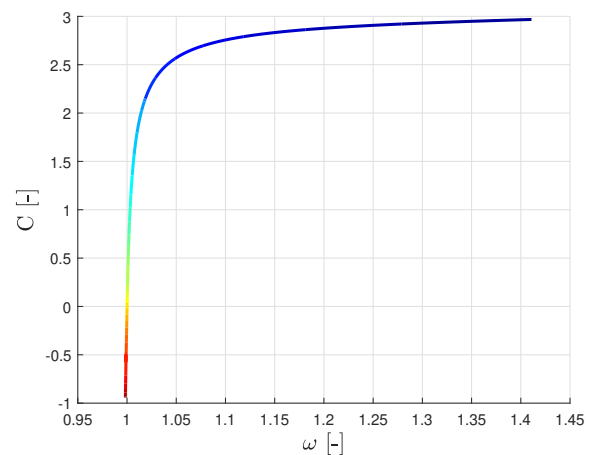


FIG. 5.15: Jacobi constant vs orbit frequency along the continuation.

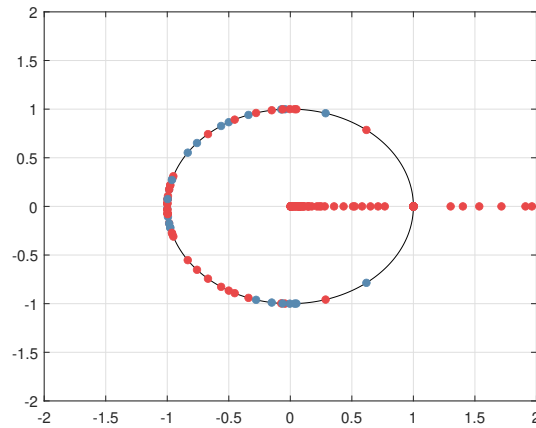


FIG. 5.16: Evolution on the complex plane of the Floquet multipliers during the continuation of the **V1** family.

As implied by the name of the family, it primarily grows in the z direction. **FIG. 5.16** shows how all the orbits are unstable due to the fact that at least one multiplier is always outside of the unit circle, and it shows no bifurcations had been detected.

With all the families around the first Lagrangian point being computed, it is now possible, in order to have a better visualisation, to present the complete connection diagram between these branches in **FIG. 5.17**.

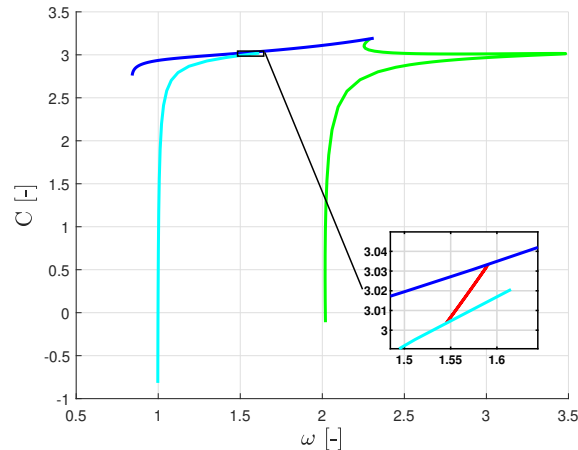


FIG. 5.17: Connection between the different family branches around the first Lagrange point.

The blue line in the graph represents the branch of Lyapunov orbits, from which the Halo in green and the Axial in red bifurcates. Finally, the Vertical family bifurcates from the Axial family and is reported in cyan in the graph.

5.2 Asteroid problem

5.2.1 Recast

The first step to approach the asteroid problem is to re-scale the equations of motion. **EQ.** 2.11 can be easily re-scaled through the use of the characteristic units of length and time defined as

$$L_0 = 2 \left(\frac{3V}{4\pi} \right)^{\frac{1}{3}}, \quad T_0 = \frac{2\pi}{\omega_a}, \quad (5.3)$$

where V is the volume of the polyhedral mesh and ω_a is the angular velocity of the asteroid. In combination to the addition of the unfolding term and making the equation to be a system of first order ode leads to

$$\begin{cases} \dot{x} = u \\ \dot{y} = v \\ \dot{z} = w \\ \dot{u} = -\lambda u + 2\omega_a T_0 v + \omega_a^2 T_0^2 x + \frac{T_0^2}{L_0} U_{/x} \\ \dot{v} = -\lambda v - 2\omega_a T_0 u + \omega_a^2 T_0^2 y + \frac{T_0^2}{L_0} U_{/y} \\ \dot{w} = -\lambda w + \frac{T_0^2}{L_0} U_{/z} \end{cases} \quad (5.4)$$

The second step consists in the recasting of the gravitational potential gradient, since **EQ.** 2.28 shows the presence of non-linearities in the L_e and ω_f terms. In order to achieve an easier recasting method, the gravitational potential gradient can be written as

$$\nabla U = \mathbf{M}_1 \mathbf{L} - \mathbf{M}_2 \mathbf{L} \otimes \mathbf{r} + \mathbf{M}_3 2\boldsymbol{\omega} - \mathbf{M}_4 2\boldsymbol{\omega} \otimes \mathbf{r}, \quad (5.5)$$

in which \mathbf{L} contains all the L_e terms from every edge, $\boldsymbol{\omega}$ all the $\frac{\omega_f}{2}$ terms from every face. \mathbf{M}_1 is a matrix whose columns are the results of $\mathbf{E}_e \mathbf{r}_{mpe}$ where \mathbf{r}_{mpe} is the medium point of the edge, \mathbf{M}_2 is a matrix built by arranging in line all the \mathbf{E}_e matrices. \mathbf{M}_3 a matrix whose column are the results of $\mathbf{F}_f \mathbf{r}_{bf}$ where \mathbf{r}_{bf} is the barycentre of the face, and finally, \mathbf{M}_4 is obtained by arranging all the \mathbf{F}_f matrices in line.

Thanks to this new expression, and the re-scaling accordingly to the introduced constants, it is possible to split the gravitational potential gradient into the edges component

$$\nabla U_e = \mathbf{M}_1 \mathbf{L} - \mathbf{M}_2 \mathbf{L} \otimes \mathbf{r}, \quad (5.6)$$

and into the faces component

$$\nabla U_f = \mathbf{M}_3 2\boldsymbol{\omega} - \mathbf{M}_4 2\boldsymbol{\omega} \otimes \mathbf{r} \quad (5.7)$$

of which the recast is simpler.

Edges auxiliary variables

For the recast of the edges component, it is necessary to introduce the following auxiliary variables for each edge of the mesh

$$\begin{cases} v_{1e} = \sqrt{\mathbf{r}_i \cdot \mathbf{r}_i} \\ v_{2e} = \sqrt{\mathbf{r}_j \cdot \mathbf{r}_j} \\ v_{3e} = \frac{v_{1e} + v_{2e} + e_{ij}}{v_{1e} + v_{2e} - e_{ij}} \\ v_{4e} = \ln(v_{3e}) \\ v_{5e} = \frac{1}{v_{3e}} \end{cases} \quad (5.8)$$

Moreover, as the non-linearity is non-polynomial, it is also necessary to introduce the differential of the 4th variable, which enables to treat the non-linearity as a quadratic one

$$dv_{4e} = v_{5e} dv_{3e}. \quad (5.9)$$

The edges component will introduce $5n_e$ auxiliary variables, where n_e is the total number of edges.

Faces auxiliary variables

The recasting of this component will add a large number of auxiliary variables, in fact, for every face it is necessary to introduce the following auxiliary variables:

$$\begin{cases} v_{1f} = \sqrt{\mathbf{r}_i \cdot \mathbf{r}_i} \\ v_{2f} = \sqrt{\mathbf{r}_j \cdot \mathbf{r}_j} \\ v_{3f} = \sqrt{\mathbf{r}_k \cdot \mathbf{r}_k} \\ v_{4f} = \mathbf{r}_j \cdot \mathbf{r}_k \\ v_{5f} = \mathbf{r}_k \cdot \mathbf{r}_i \\ v_{6f} = \mathbf{r}_i \cdot \mathbf{r}_j \\ v_{7f} = (\mathbf{r}_j \times \mathbf{r}_k)_x \\ v_{8f} = (\mathbf{r}_j \times \mathbf{r}_k)_y \\ v_{9f} = (\mathbf{r}_j \times \mathbf{r}_k)_z \\ v_{10f} = v_{1f} v_{2f} \\ v_{11f} = v_{10f} v_{3f} + v_{1f} v_{4f} + v_{2f} v_{5f} + v_{3f} + v_{6f} \\ v_{12f} = \frac{\mathbf{r}_{ix} v_{7f} + \mathbf{r}_{iy} v_{8f} + \mathbf{r}_{iz} v_{9f}}{v_{11f}} \\ v_{13f} = \arctan(v_{12f}) \\ v_{14f} = 1 + v_{12f}^2 \\ v_{15f} = \frac{1}{v_{14f}} \end{cases} \quad (5.10)$$

As for the edges component case, the non-linearity is non-polynomial and there is the necessity to introduce the differential form of the 13th variable

$$dv_{13f} = v_{15f} dv_{12f}. \quad (5.11)$$

In total, the faces component recasting would add a total of $15n_f$ auxiliary variables, where n_f is the total number of faces present in the polyhedron mesh.

Therefore, the recasting of the asteroid problem, due to the complex nature of the gravitational potential gradient expression, requires a total number of $5n_e + 15n_f$ auxiliary variables.

In many cases, asteroid meshes can have a high number of edges and faces, as shown in **TAB. 5.1**.

TAB. 5.1 Necessary auxiliary variables for asteroid meshes.

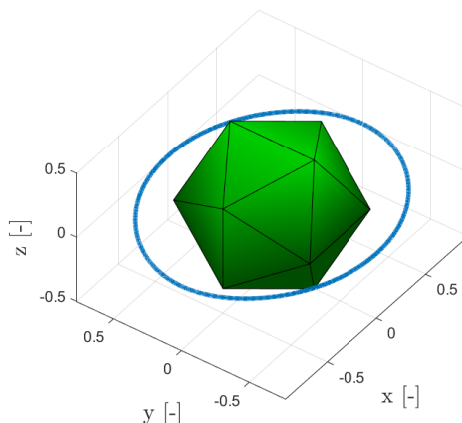
Asteroid	n_e	n_f	n_{aux}
1996 Hw1	4170	2780	62550
4769 Castalia	6138	4092	92070
6489 Golevka	6138	4092	92070
433 Eros	2562	1708	38430

For this reason an ordinary computer doesn't have access to enough memory to handle such problems or to find solutions in a reasonable amount of time.

Therefore, in order to check if the software works for this problem as well, the computation in this section was performed on an icosphere mesh having 30 edges and 20 faces.

5.2.2 Icosphere

The mesh under study has a density $\rho = 2700 \text{ Kg/m}^3$ and an angular velocity $\omega_a = 1.99 \cdot 10^{-4} \text{ rad/s}$, and it is shown in **FIG. 5.18** along with the starting periodic orbit obtained with the **HBM**.

**FIG. 5.18:** Icosphere mesh and starting periodic orbit.

By applying the continuation procedure for a total of 35 steps, and taking into account only 30 harmonics contributions for the Fourier development, it was possible to obtain the orbit family shown in **FIG. 5.19**. It is important to note that the residue managed to converge to a value of $R = 10^{-8}$ at the first step of the continuation by means of 10 Newton-Raphson corrections iterations. However, for every remaining step the correction was not performed as the residue naturally remained within the 10^{-8} range.

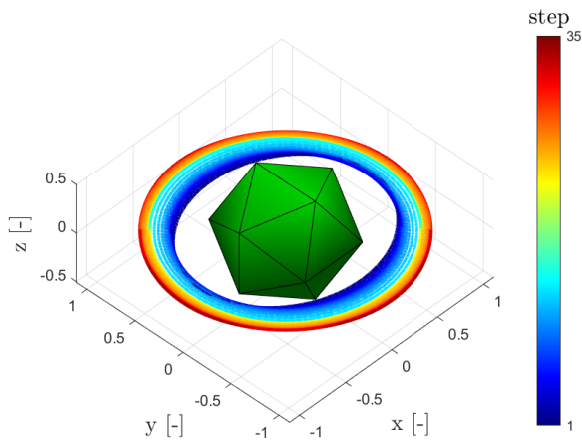


FIG. 5.19: Icosphere orbit family computed through ManLab.

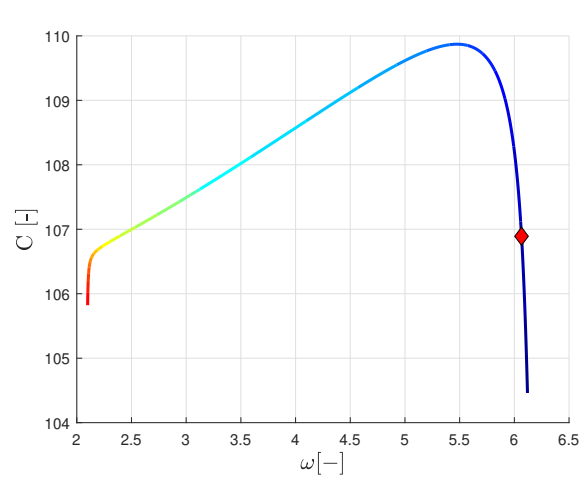


FIG. 5.20: Jacobi constant vs orbit frequency along the continuation.

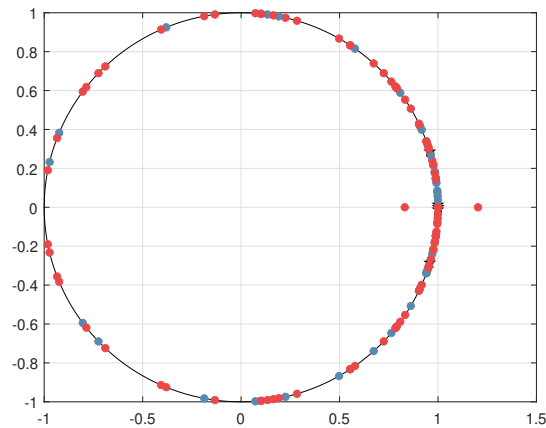


FIG. 5.21: Evolution on the complex plane of the Floquet multipliers.

FIG. 5.21 shows that a tangent bifurcation, with change of stability from unstable to stable was detected. The position of the bifurcation is reported as well in **FIG. 5.20**, from which can be easily seen that it occurred rather early during the continuation at $\omega = 6.0657$. After this bifurcations, the multipliers moved along the circumference towards the -1 point.

In order to check the if those orbits correspond to the real ones, it is useful to compare them with orbits obtained by integrating in time the initial conditions taken from the ManLab orbits, as it was done before for the two-body problem.

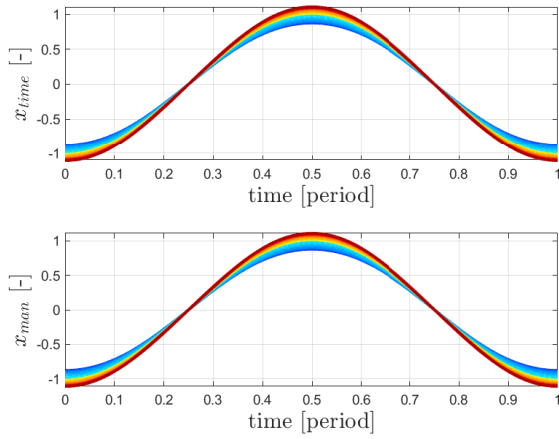


FIG. 5.22: Trajectory x component computed through time integration and through ManLab.

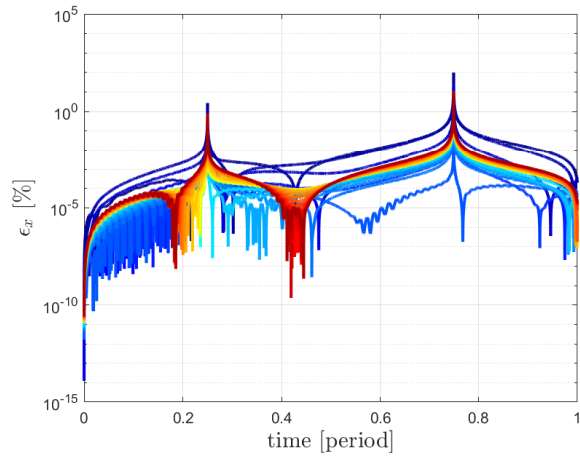


FIG. 5.23: Percentage relative error on the x component between the two methods.

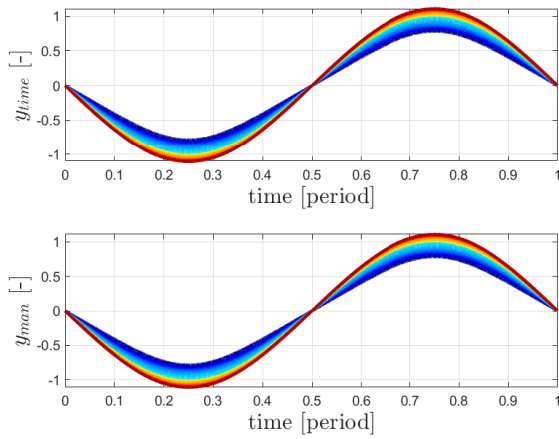


FIG. 5.24: Trajectory y component computed through time integration and through ManLab.

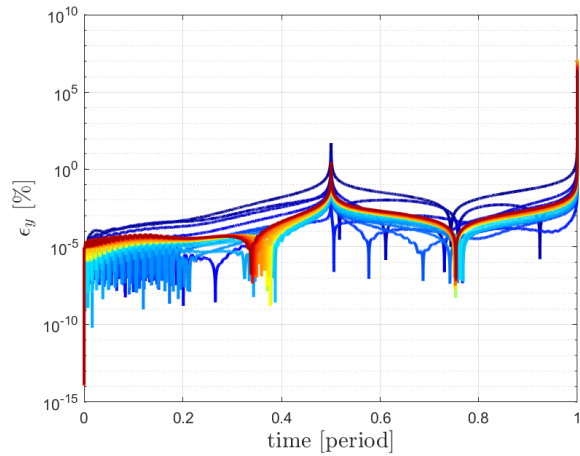


FIG. 5.25: Percentage relative error on the y component between the two methods.

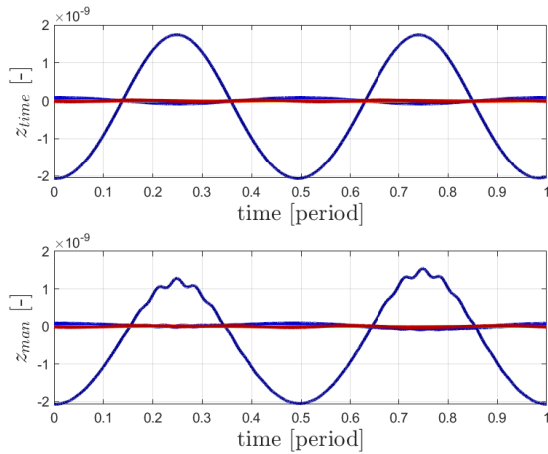


FIG. 5.26: Trajectory z component computed through time integration and through ManLab.

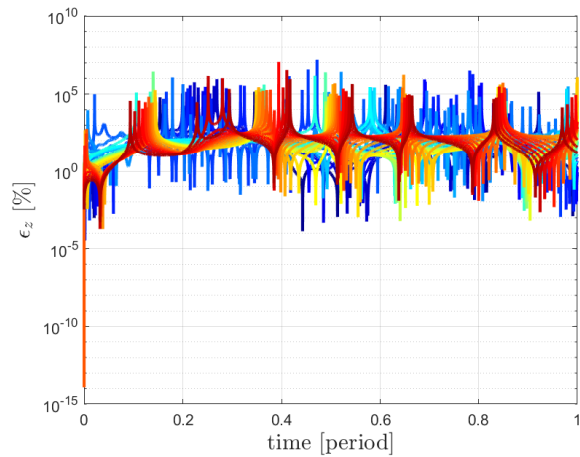


FIG. 5.27: Percentage relative error on the z component between the two methods.

Interestingly, figures from **FIG. 5.22** to **FIG. 5.25** show that the x and y component of the trajectory almost coincide for both methods. Furthermore, **FIG. 5.26** and **FIG. 5.27** demonstrate how the error becomes important if the component of interest is small. In fact in this case, the higher frequency components of the dynamics that were truncated became more significant. This error can be easily lowered by considering more frequency contributions in the Fourier decomposition.

It is finally possible to assess the difference between the results obtained through ManLab and through the **HBM** as described in Section 2.3.1.

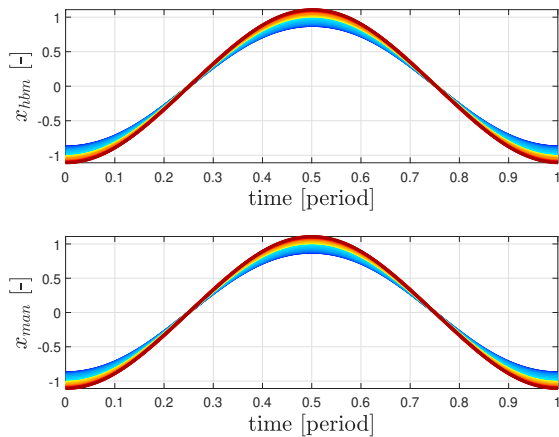


FIG. 5.28: Trajectory x component computed through **HBM** and through ManLab.

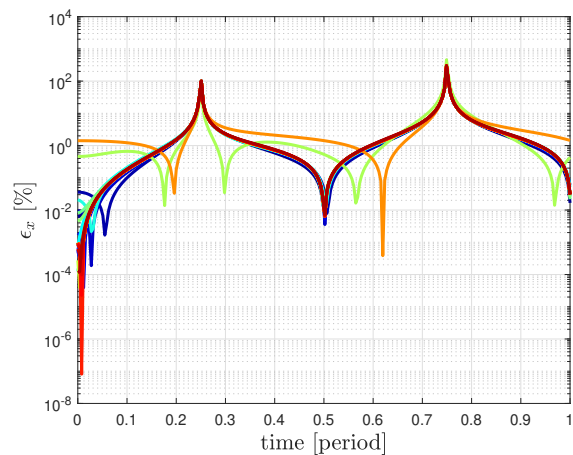


FIG. 5.29: Percentage relative error on the x component between the two methods.

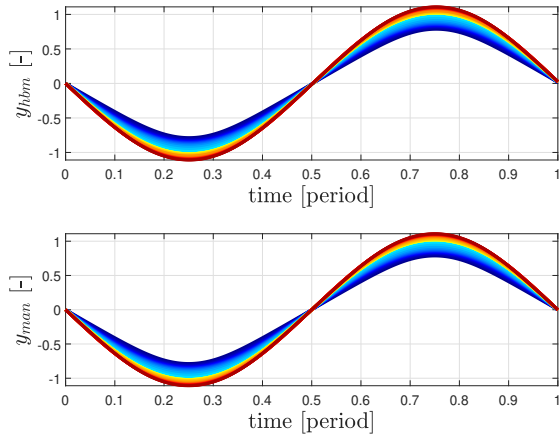


FIG. 5.30: Trajectory y component computed through **HBM** and through ManLab.

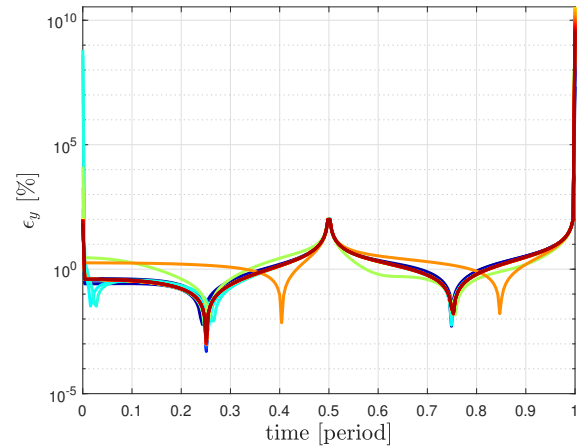


FIG. 5.31: Percentage relative error on the y component between the two methods.

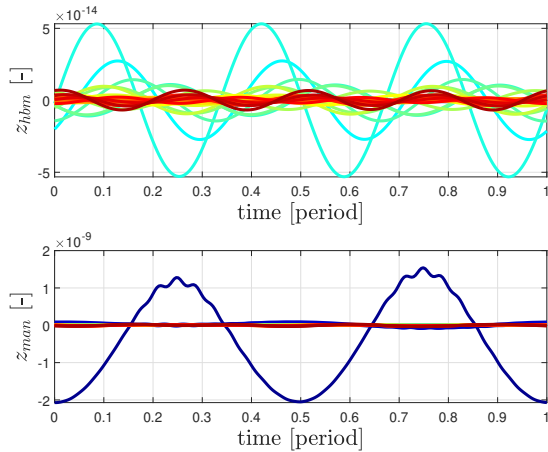


FIG. 5.32: Trajectory z component computed through **HBM** and through ManLab.

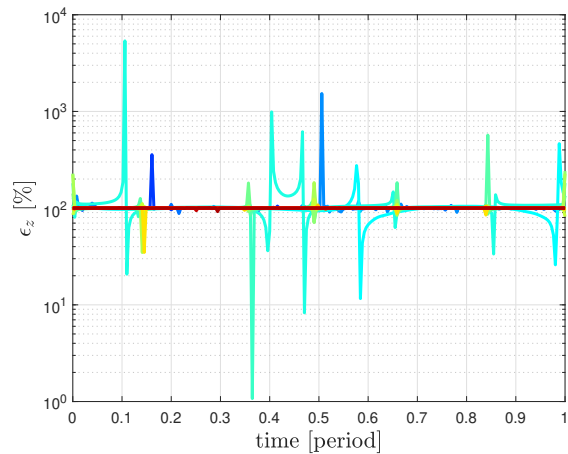


FIG. 5.33: Percentage relative error on the z component between the two methods.

Figures from **FIG. 5.28** to **FIG. 5.33** show that the trajectories computed with the two frequency methods are almost coinciding, with the relative error being contained for almost all the period duration and with the maximum difference happening at the extreme points for the x and y components of the trajectories. Instead, for the z components, the **HBM** was able to get closer to zero, therefore the relative error gets relatively high.

The here presented comparison between the time integration and the **HBM** gives sufficient evidence to confirm that the software is computing corrects orbits.

Branching solutions

As ManLab is capable to automatically detect bifurcation points, it is possible to follow different branches of the solution by imposing these as starting points of the following continuation steps. By setting a stricter tolerance on the residue ($R = 10^{-11}$) to the family in **FIG. 5.19** and applying

Newton-Raphson correction at each step, it was possible to detect another tangent bifurcation at $\omega = 3.143$, shown in **FIG. 5.35**.

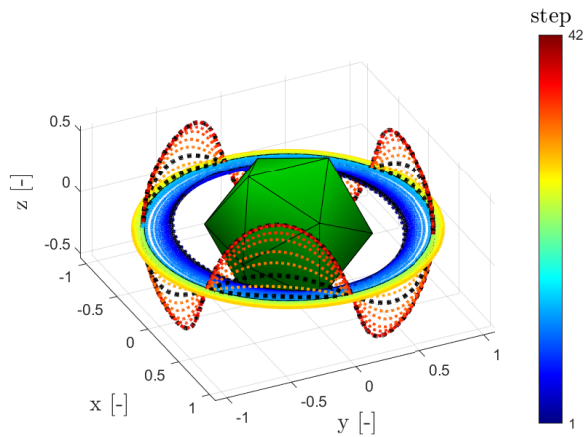


FIG. 5.34: Icosphere orbit family computed through ManLab.

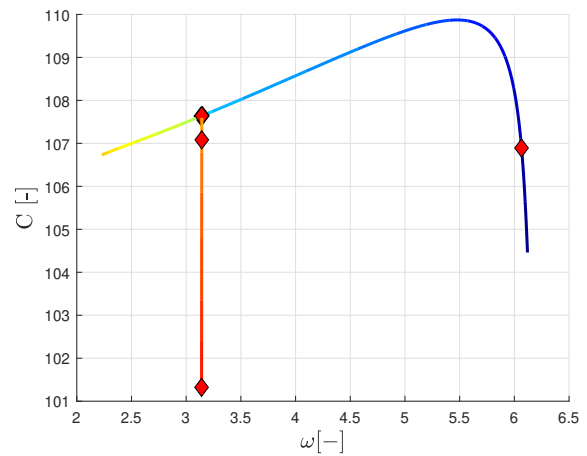


FIG. 5.35: Jacobi constant vs orbit frequency along the continuation.

FIG. 5.34 reports a representation of the family belonging to the main branch and of the family emerging from it. Orbits represented by a continuous line are stable while the ones represented with a dashed line are unstable. Finally, orbits in black is where a change of stability or a branching point is detected.

It can not only be seen that the main family is stable and the emerging one is unstable, but also that the family has a constant frequency with a decreasing Jacobi constant.

Therefore, by selecting appropriate tolerances and Newton-Raphson corrections, it is possible not only to detect branches points but also to follow them instead of the main branch, without the necessity of restarting the computations and without any re-initialisation. This is a strong advantage of the method, it make possible to study in a more efficient way the complete bifurcation diagram of the orbits around an irregular body.

Conclusions and future development

In this work, the open source ManLab was adopted to compute and continue periodic orbits in the circular restricted three body problem environment and in the environment around irregularly-shaped uniform-rotating asteroids. The work aimed to assess the validity of the well known **HBM** when being applied to a novel problem for the algorithm. Unlike to the currently used method, the **HBM** approaches the problem in the frequency domain, representing a more powerful and efficient method with respect to the other commonly used methods.

To accomplish the objective, the dynamics within the aforementioned environments were studied, particularly focus on the choice of the appropriate model to compute the gravity field around irregular-shaped bodies.

The theory behind both the **HBM** and its quadratic implementation in ManLab was documented. Two simple examples consisting in a forced Van der Pol oscillator and in a free pendulum were examined in order to demonstrate the initialisation step for the continuation within the software and to show quadratic recast of the equations of motion, since these two are the most cumbersome passages for achieving good results and that could take the most time of the analysis. Furthermore, the Keplerian two body problem motion was used in order to assess the validity of the gravitational potential, as well as the correctness of the computations of the software. In addition, it served to check if the initialisation and quadratic recast procedures works for a more complex problem as well.

Therefore, through the analysis of the orbit families around the L_1 Lagrangian point and using an appropriate number of harmonics in the truncated Fourier development, it could be concluded that the method is well suited for the resolution of the circular restricted three body problem.

It was finally found that the method, after an adequate recast, is well capable of solving the problem around irregular-shaped bodies as well. However to demonstrate this a fictitious body was used to carry out the computation, as real existing bodies require computational power well beyond the available one in an ordinary computer. Using this body, it was possible to assess the equivalency of the results computed through ManLab, time integration and the **HBM**. Furthermore, the possibility to follow other branches was also proven for this case.

This work provides a proof of concept and builds the bases for further developments such as: the analysis of periodic and quasi-periodic motion for both real asteroids and the **CR3BP** by using a computer having more available computational power. Moreover, in order to compute faster the results the method can be integrated for parallel computation and non-linear reduction methods can be applied to the equations of motion of the problem of interest.

References

- [1] Tycho T Von Rosenvinge, John C Brandt, and Robert W Farquhar. “The international cometary explorer mission to comet Giacobini-Zinner”. In: *Science* 232.4748 (1986), pp. 353–356.
- [2] Roald Z Sagdeev et al. “Vega spacecraft encounters with comet Halley”. In: *Nature* 321.Suppl 6067 (1986), pp. 259–262.
- [3] R Reinhard. “The Giotto encounter with comet Halley”. In: *Nature* 321.Suppl 6067 (1986), pp. 313–318.
- [4] TV Johnson, CM Yeates, and R Young. “Space science reviews volume on Galileo mission overview”. In: *The Galileo Mission* (1992), pp. 3–21.
- [5] J Veverka et al. “The landing of the NEAR-Shoemaker spacecraft on asteroid 433 Eros”. In: *Nature* 413.6854 (2001), pp. 390–393.
- [6] Jun’ichiro Kawaguchi, Akira Fujiwara, and Tono Uesugi. “Hayabusa—Its technology and science accomplishment summary and Hayabusa-2”. In: *Acta Astronautica* 62.10-11 (2008), pp. 639–647.
- [7] Don Brownlee. “The Stardust mission: analyzing samples from the edge of the solar system”. In: *Annual Review of Earth and Planetary Sciences* 42 (2014), pp. 179–205.
- [8] Karl-Heinz Glassmeier et al. “The Rosetta mission: flying towards the origin of the solar system”. In: *Space Science Reviews* 128 (2007), pp. 1–21.
- [9] Yuichi Tsuda et al. “System design of the Hayabusa 2—Asteroid sample return mission to 1999 JU3”. In: *Acta Astronautica* 91 (2013), pp. 356–362.
- [10] DS Lauretta et al. “OSIRIS-REx: sample return from asteroid (101955) Bennu”. In: *Space Science Reviews* 212 (2017), pp. 925–984.
- [11] Mr Monte Henderson and Mr William Blume. “Deep Impact—A Review of the World’s Pioneering Hypervelocity Impact Mission”. In: *Procedia Engineering* 103 (2015), pp. 165–172.
- [12] Andrew F Cheng et al. “Momentum transfer from the DART mission kinetic impact on asteroid Dimorphos”. In: *Nature* (2023), pp. 1–3.
- [13] Patrick Michel, Michael Küppers, and Ian Carnelli. “The Hera mission: European component of the ESA-NASA AIDA mission to a binary asteroid”. In: *42nd COSPAR Scientific Assembly* 42 (2018), B1–1.
- [14] Harold F Levison et al. “Lucy mission to the Trojan asteroids: Science goals”. In: *The Planetary Science Journal* 2.5 (2021), p. 171.
- [15] LT Elkins-Tanton et al. “Asteroid (16) Psyche: Visiting a metal world”. In: (2017).
- [16] X Zhang et al. “ZhengHe—a mission to a near-earth asteroid and a main belt comet”. In: *50th Annual Lunar and Planetary Science Conference*. 2132. 2019, p. 1045.
- [17] NASA. *NEO Surveyor*. <https://www.jpl.nasa.gov/missions/near-earth-object-surveyor>.
- [18] T Arai et al. “DESTINY+ mission: Flyby of Geminids parent asteroid (3200) Phaethon and in-situ analyses of dust accreting on the Earth”. In: *49th Annual Lunar and Planetary Science Conference*. 2083. 2018, p. 2570.

- [19] Joan Pau Sánchez et al. “ESA F-Class Comet Interceptor: Trajectory design to intercept a yet-to-be-discovered comet”. In: *Acta Astronautica* 188 (2021), pp. 265–277.
- [20] Leclère Nicolas, Kerschen Gaëtan, et al. “Multiple bifurcations around 433 Eros with Harmonic Balance Method”. In: *Proceedings of the International Astronomical Union* 15.S364 (2021), pp. 171–177.
- [21] D.J. Scheeres et al. “Orbits Close to Asteroid 4769 Castalia”. In: *Icarus* 121.1 (1996), pp. 67–87.
- [22] Daniel J Scheeres. *Orbital motion in strongly perturbed environments: applications to asteroid, comet and planetary satellite orbiters*. Springer, 2016.
- [23] Yu Jiang et al. “Orbits and manifolds near the equilibrium points around a rotating asteroid”. In: *Astrophysics and Space Science* 349 (2014), pp. 83–106.
- [24] Yu Jiang, Hexi Baoyin, and Hengnian Li. “Periodic motion near the surface of asteroids”. In: *Astrophysics and Space Science* 360 (2015), pp. 1–10.
- [25] R Broucke and Antonio Elipe. “The dynamics of orbits in a potential field of a solid circular ring”. In: *Regular and Chaotic Dynamics* 10.2 (2005), pp. 129–143.
- [26] Angelo Alberti and Claudio Vidal. “Dynamics of a particle in a gravitational field of a homogeneous annulus disk”. In: *Celestial Mechanics and Dynamical Astronomy* 98 (2007), pp. 75–93.
- [27] Xiaodong Liu, Hexi Baoyin, and Xingrui Ma. “Periodic orbits in the gravity field of a fixed homogeneous cube”. In: *Astrophysics and Space Science* 334 (2011), pp. 357–364.
- [28] Xiangyu Li, Dong Qiao, and Pingyuan Cui. “The equilibria and periodic orbits around a dumbbell-shaped body”. In: *Astrophysics and Space Science* 348 (2013), pp. 417–426.
- [29] Volodymyr A Romanov and Eusebius J Doedel. “Periodic orbits associated with the libration points of the massive rotating straight segment”. In: *International Journal of Bifurcation and Chaos* 24.04 (2014).
- [30] Lei Lan et al. “Retrograde near-circular periodic orbits near equatorial planes of small irregular bodies”. In: *Astrophysics and Space Science* 362 (2017), pp. 1–13.
- [31] William Duncan MacMillan. *The theory of the potential*. 1958.
- [32] PC Kammeyer. “Periodic orbits around a rotating ellipsoid”. In: *Celestial mechanics* 17.1 (1978), pp. 37–48.
- [33] Robert A Werner and Daniel J Scheeres. “Exterior gravitation of a polyhedron derived and compared with harmonic and mascon gravitation representations of asteroid 4769 Castalia”. In: *Celestial Mechanics and Dynamical Astronomy* 65 (1996), pp. 313–344.
- [34] TGG Chanut, Safwan Aljbaae, and V Carruba. “Mascon gravitation model using a shaped polyhedral source”. In: *Monthly Notices of the Royal Astronomical Society* 450.4 (2015), pp. 3742–3749.
- [35] William Duncan MacMillan. *The theory of the potential*. McGraw-Hill Book Company, Incorporated, 1958.
- [36] Greg Friegee. *3D Asteroid Catalogue*. URL: <https://3d-asteroids.space/>.
- [37] Dionysios Karydis, George Voyatzis, and Kleomenis Tsiganis. “A continuation approach for computing periodic orbits around irregular-shaped asteroids. An application to 433 Eros”. In: *Advances in Space Research* 68.11 (2021), pp. 4418–4433.

- [38] Fabio Ferrari. “Non-Keplerian models for mission analysis scenarios about small solar system bodies”. In: (2017).
- [39] NASA. *Three-Body Periodic Orbits*. URL: https://ssd.jpl.nasa.gov/tools/periodic_orbits.html.
- [40] VV Markellos. “Numerical investigation of the planar restricted three-body problem: II: Regions of stability for retrograde satellites of Jupiter as determined by periodic orbits of the second generation”. In: *Celestial mechanics* 10.1 (1974), pp. 87–134.
- [41] Yang Yu and Hexi Baoyin. “Generating families of 3D periodic orbits about asteroids”. In: *Monthly Notices of the Royal Astronomical Society* 427.1 (2012), pp. 872–881.
- [42] Kathleen Connor Howell. “Three-dimensional, periodic, ‘halo’ orbits”. In: *Celestial mechanics* 32.1 (1984), pp. 53–71.
- [43] T. Detroux. *Performance and robustness of nonlinear systems using bifurcation analysis*. 2016.
- [44] R. Seydel. *Practical bifurcation and stability analysis*. Springer Science & Business Media, 2009.
- [45] G. VON GROLL and D. J. EWINS. “THE HARMONIC BALANCE METHOD WITH ARC-LENGTH CONTINUATION IN ROTOR/STATOR CONTACT PROBLEMS”. In: *Journal of Sound and Vibration* 241.2 (2001), pp. 223–233.
- [46] Gerald Moore. “Floquet theory as a computational tool”. In: *SIAM journal on numerical analysis* 42.6 (2005), pp. 2522–2568.
- [47] Beatrice Meini. “A “shift-and-deflate” technique for quadratic matrix polynomials”. In: *Linear Algebra and its Applications* 438.4 (2013), pp. 1946–1961.
- [48] Y. Ni, Y. Jiang, and H. Baoyin. “Multiple bifurcations in the periodic orbit around Eros”. In: *Astrophysics and Space Science* 361 (2016), pp. 1–15.
- [49] Marie-Christine Pauszin et al. “High order harmonic balance formulation of free and encapsulated microbubbles”. In: *Journal of Sound and Vibration* 330.5 (2011), pp. 987–1004.
- [50] Marielle Debeurre et al. “Finite element computation of nonlinear modes and frequency response of geometrically exact beam structures”. In: *Journal of Sound and Vibration* 548 (2023), p. 117534.
- [51] JC Pan et al. “Modal interactions of a dual-joint cylindrical shell system via Nonlinear Normal Modes”. In: *International Journal of Mechanical Sciences* 234 (2022), p. 107659.
- [52] Gabriel Hurel, Sébastien Baguet, and Claude-Henri Lamarque. “Neimark Sacker bifurcations and non-linear energy exchange in chains of non-linear oscillators”. In: *International Journal of Non-Linear Mechanics* 144 (2022), p. 104057.
- [53] Emmanuel Cottanceau et al. “A finite element/quaternion/asymptotic numerical method for the 3D simulation of flexible cables”. In: *Finite Elements in Analysis and Design* 139 (2018), pp. 14–34.
- [54] V. Mahe et al. “Dynamic stability of centrifugal pendulum vibration absorbers allowing a rotational mobility”. In: *Journal of Sound and Vibration* 517 (2022), p. 116525.
- [55] Mahe V et al. “On the dynamic stability and efficiency of centrifugal pendulum vibration absorbers with rotating pendulums”. In: *Journal of Sound and Vibration* 536 (2022), p. 117157.
- [56] ManLab. 2019. URL: <http://manlab.lma.cnrs-mrs.fr/spip.php?rubrique1>.

- [57] MathWorks. *MATLAB*. 2023. URL: <https://it.mathworks.com/products/matlab.html>.
- [58] N.Damil and M.Potier-Ferry. “A New method to compute perturbed bifurcations: Application to the buckling of imperfect elastic structures”. In: *International Journal of Engineering Science* 28.9 (1990), pp. 943–957.
- [59] B.Cochelin, N.Damil, and M.Potier-Ferry. “Asymptotic numerical methods and pade approximants for non-linear elastic structures”. In: *International journal for numerical methods in engineering* 37 (1994), pp. 1187–1213.
- [60] B.Cochelin C.Vergez. “A high order purely frequency-based harmonic balance formulation for continuation of periodic solutions”. In: *Journal of sound and vibration* 324.1-2 (2009), pp. 243–262.
- [61] S. Karkar, B.Cochelin, and C.Vergez. “A high-order, purely frequency based harmonic balance formulation for continuation of periodic solutions: The case of non-polynomial nonlinearities”. In: *Journal of Sound and Vibration* 332.4 (2013), pp. 968–977.
- [62] E.Cottanceau et al. “A finite element/quaternion/asymptotic numerical method for the 3D simulation of flexible cables”. In: *Finite Elements in Analysis and Design* 139 (2018), pp. 14–34.
- [63] H. Zahrouni, B. Cochelin, and M. Potier-Ferry. “Computing finite rotations of shells by an asymptotic-numerical method”. In: *Computer Methods in Applied Mechanics and Engineering* 175.1 (1999), pp. 71–85.
- [64] L.Guillot, B.Cochelin, and C.Vergez. “A generic and efficient Taylor series-based continuation method using a quadratic recast of smooth nonlinear systems”. In: *International Journal for numerical methods in Engineering* 119.4 (2019), pp. 261–280.
- [65] B. Cochelin. “A path-following technique via an asymptotic-numerical method”. In: *Computers and Structures* 53.5 (1994), pp. 1181–1192.
- [66] Louis Guillot et al. “A purely frequency based Floquet-Hill formulation for the efficient stability computation of periodic solutions of ordinary differential systems”. In: *Journal of Computational Physics* 416 (2020).
- [67] Francisco J Munoz-Almaraz et al. “Continuation of periodic orbits in conservative and Hamiltonian systems”. In: *Physica D: Nonlinear Phenomena* 181.1-2 (2003), pp. 1–38.
- [68] Xianyu Wang, Yu Jiang, and Shengping Gong. “Analysis of the potential field and equilibrium points of irregular-shaped minor celestial bodies”. In: *Astrophysics and Space Science* 353 (2014), pp. 105–121.

Families around L_2 and L_3 Lagrange Point

A.1 Families around L_2

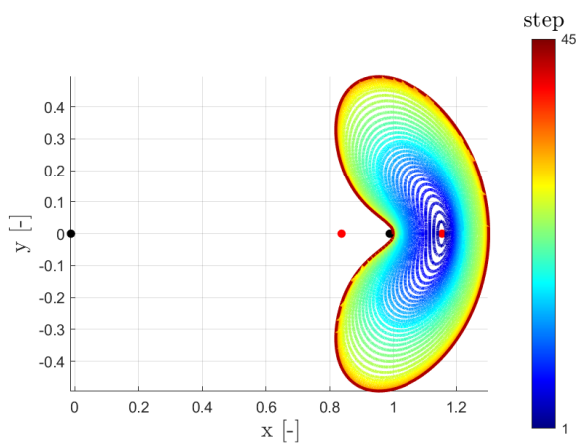


FIG. A.1: L2 family computed through ManLab accounting 200 harmonics.

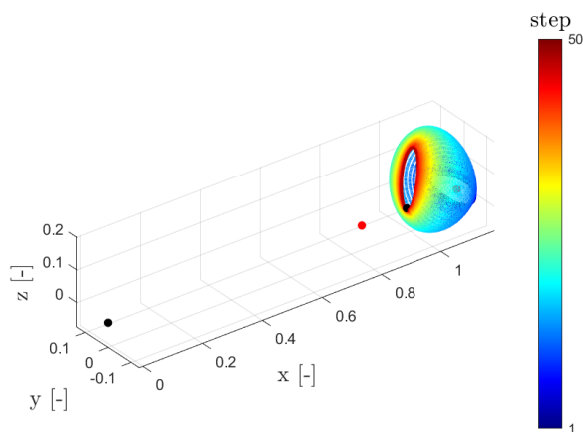


FIG. A.2: H2 family computed through ManLab accounting 200 harmonics.

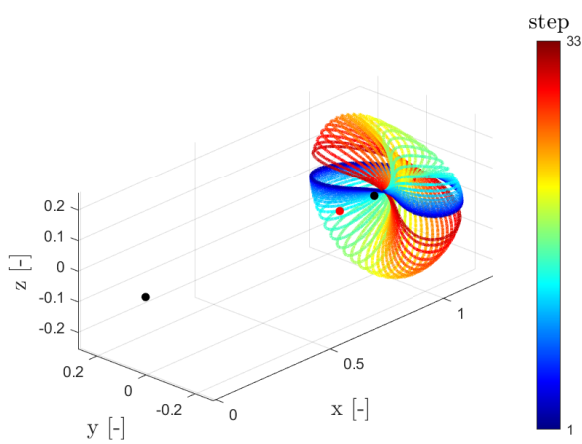


FIG. A.3: A2 family computed through ManLab accounting 200 harmonics.

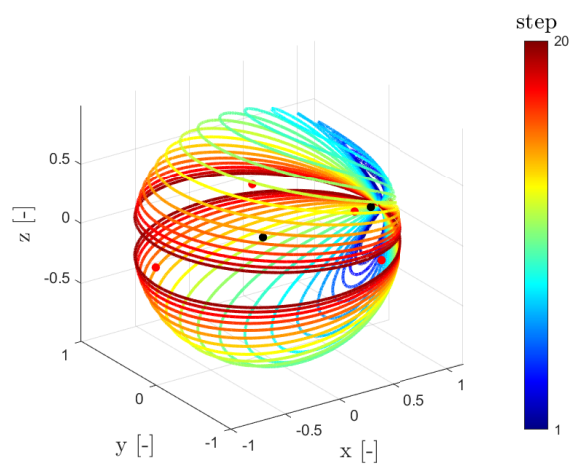


FIG. A.4: V2 family computed through ManLab accounting 200 harmonics.

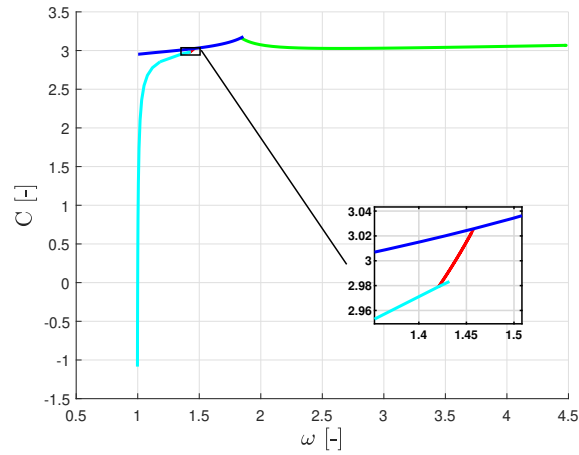


FIG. A.5: Connection between the different family branches around the second Lagrange point.

FIG. A.5 shows the connection between the branches of the orbits around the second Lagrange point. Lyapunov family is shown in blue, Halo in green, Axial in red and Vertical in cyan.

A.2 Families around L_3

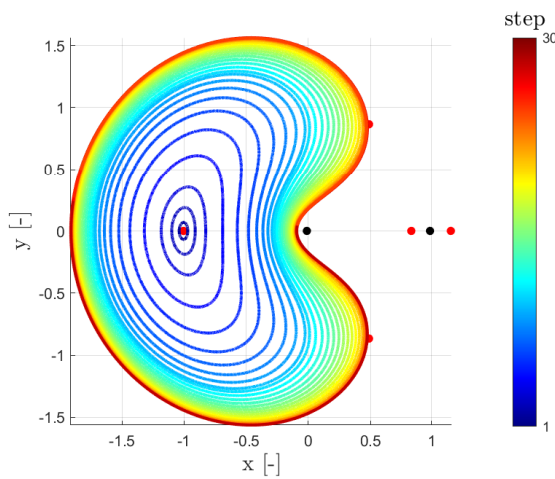


FIG. A.6: L2 family computed through ManLab accounting 200 harmonics.

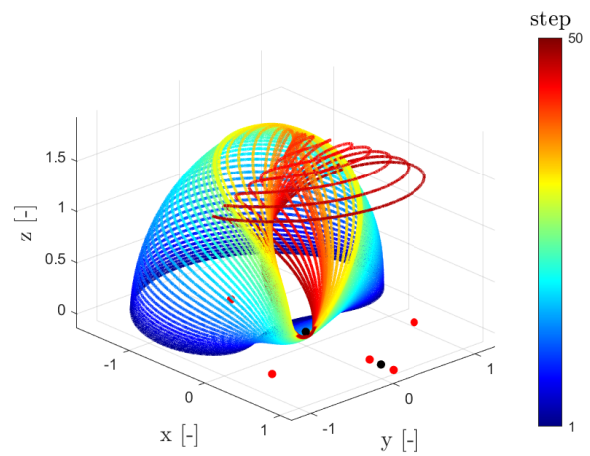


FIG. A.7: H3 family computed through ManLab accounting 200 harmonics.

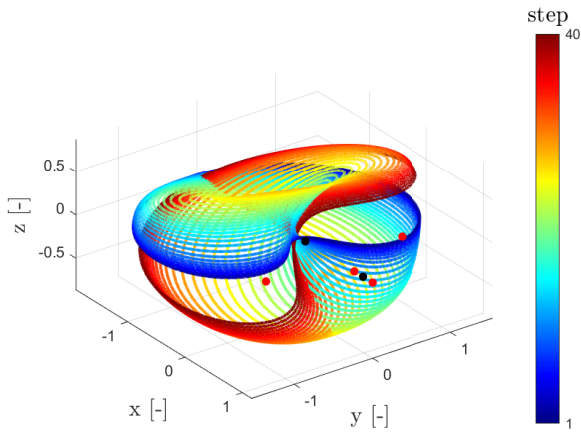


FIG. A.8: A3 family computed through ManLab accounting 250 harmonics.

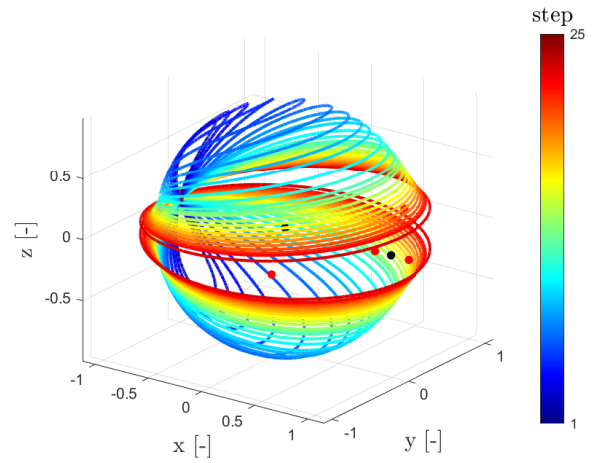


FIG. A.9: V3 family computed through ManLab accounting 200 harmonics.

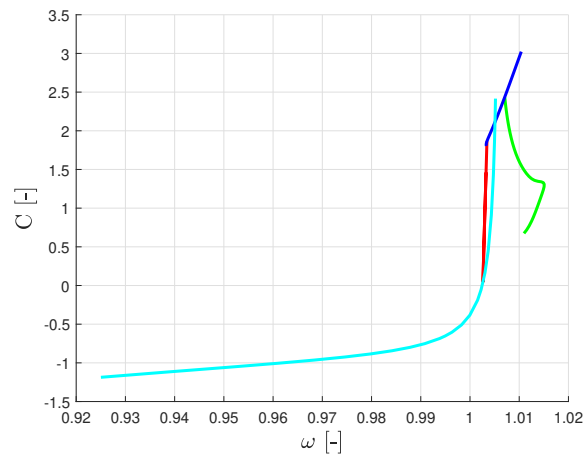


FIG. A.10: Connection between the different family branches around the third Lagrange point.

FIG. A.10 shows the connection between the branches of the orbits around the second Lagrange point. Lyapunov family is shown in blue, Halo in green, Axial in red and Vertical in cyan.